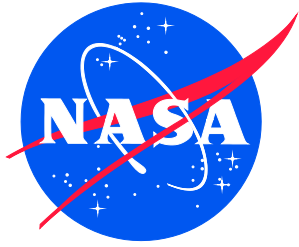# Design and Analysis of Buckling-Critical Large-Scale Sandwich Composite Cylindrical Test Articles

Adam Przekop, Marc R. Schultz, Cyrus J. R. Kosztowny, Kyongchan Song, Michael C. Lindell, and Mark W. Hilburger
Langley Research Center, Hampton, Virginia

Michelle T. Rudd
Marshall Space Flight Center, Huntsville, Alabama

November 2020

NASA STI Program . . . in Profile

Since its founding, NASA has been dedicated to the advancement of aeronautics and space science. The NASA scientific and technical information (STI) program plays a key part in helping NASA maintain this important role.

The NASA STI program operates under the auspices of the Agency Chief Information Officer. It collects, organizes, provides for archiving, and disseminates NASA's STI. The NASA STI program provides access to the NTRS Registered and its public interface, the NASA Technical Reports Server, thus providing one of the largest collections of aeronautical and space science STI in the world. Results are published in both non-NASA channels and by NASA in the NASA STI Report Series, which includes the following report types:

- TECHNICAL PUBLICATION. Reports of completed research or a major significant phase of research that present the results of NASA Programs and include extensive data or theoretical analysis. Includes compilations of significant scientific and technical data and information deemed to be of continuing reference value. NASA counter-part of peer-reviewed formal professional papers but has less stringent limitations on manuscript length and extent of graphic presentations.

- TECHNICAL MEMORANDUM. Scientific and technical findings that are preliminary or of specialized interest, e.g., quick release reports, working papers, and bibliographies that contain minimal annotation. Does not contain extensive analysis.

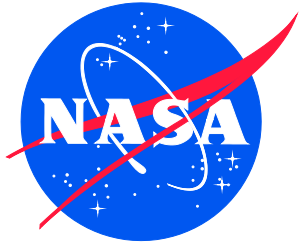- CONTRACTOR REPORT. Scientific and technical findings by NASA-sponsored contractors and grantees.

- CONFERENCE PUBLICATION. Collected papers from scientific and technical conferences, symposia, seminars, or other meetings sponsored or co-sponsored by NASA.

- SPECIAL PUBLICATION. Scientific, technical, or historical information from NASA programs, projects, and missions, often concerned with subjects having substantial public interest.

- TECHNICAL TRANSLATION. English-language translations of foreign scientific and technical material pertinent to NASA's mission.

Specialized services also include organizing and publishing research results, distributing specialized research announcements and feeds, providing information desk and personal search support, and enabling data exchange services.

For more information about the NASA STI program, see the following:

- Access the NASA STI program home page at *http://www.sti.nasa.gov*

- E-mail your question to help@sti.nasa.gov

- Phone the NASA STI Information Desk at 757-864-9658

- Write to:
  NASA STI Information Desk
  Mail Stop 148
  NASA Langley Research Center
  Hampton, VA 23681-2199

Design and Analysis of Buckling-Critical Large-Scale Sandwich Composite Cylindrical Test Articles

Adam Przekop, Marc R. Schultz, Cyrus J. R. Kosztowny, Kyong C. Song,
Michael C. Lindell, and Mark W. Hilburger
Langley Research Center, Hampton, Virginia

Michelle T. Rudd
Marshall Space Flight Center, Huntsville, Alabama

Acknowledgements

Available from:

NASA Center for AeroSpace Information
7115 Standard Drive
Hanover, MD 21076-1320
443-757-5802

Table of Contents

List of Figures

List of Tables

Nomenclature

A_{11}, A_{22}	Membrane stiffnesses in the axial and circumferential directions, respectively
A_{66}	In-plane shear stiffness
A_{ij}	Membrane stiffnesses
A_{ij}^f	Facesheet membrane stiffnesses
CTA8.x	8-ft-diameter composite test article designation where x is the specimen identification
D_{11}, D_{22}	Bending stiffnesses in the axial and circumferential directions, respectively
D_{66}	In-plane twisting stiffness
D_{ij}	Bending stiffnesses
D	Cylinder midsurface diameter
d	Honeycomb-core cell size
E_c	Effective core transverse shear modulus
E_x, E_y	Potting-material extensional moduli in the axial and circumferential directions, respectively
$\bar{E}_x, \bar{E}_y$	Effective facesheet extensional moduli in the axial and circumferential directions, respectively
E_0	Axial direction extensional modulus
E_{11}, E_{22}	In-plane extensional moduli in the fiber and matrix directions, respectively
FAW	Fiber areal weight
FEA	Finite element analysis
FEM	Finite element model
G_{12}	In-plane shear modulus
G_{13}, G_{23}	Transverse shear moduli in the axial and circumferential directions, respectively
G_{xz}	Core transverse shear modulus in the axial-transverse plane
h	Midsurface distance between facesheets ($t_f + t_c$)
IML	Inner mold line
KD	Co-cure knockdown factor
L	Cylinder length
MSFC	Marshall Space Flight Center
NESC	NASA Engineering and Safety Center
OML	Outer mold line
P_{cr}	Global buckling load, defined by Eq. (4)
P_{CS}	Core-shear-instability load, defined by Eq. (11)
P_{FD}	Facesheet dimpling load, defined by Eq. (10)
P_{FW}	Facesheet wrinkling load, defined by Eq. (9)
pcf	Pounds per cubic foot
R	Cylinder midsurface radius
S	In-plane shear lamina strength
SBKF	Shell Buckling Knockdown Factor Project
t	Shell thickness
t_{eff}	Effective thickness, defined by Eq. (1)
t_c	Core thickness
t_f	Facesheet thickness
t_p	Cured ply thickness
V	Volume fraction
X_c	Compressive lamina strength in fiber direction
X_t	Tensile lamina strength in fiber direction
Y_c	Compressive lamina strength in direction perpendicular to fiber
Y_t	Tensile lamina strength in direction perpendicular to fiber

ε_{cr}	Axial membrane strain at P_{cr} defined by Eq. (8)
ε_x	Angle-ply laminate axial strain at failure
ϕ	Nondimensional parameter in Eq. (4), defined by Eq. (5)
ν	Poisson's ratio
$\bar{\nu}_{xy}, \bar{\nu}_{yx}$	Effective facesheet in-plane Poisson's ratios
ν_{12}	In-plane Poisson's ratio
ν_{13}, ν_{23}	Axial-transverse and circumferential-transverse Poisson's ratios, respectively
σ	Compressive strength of facesheet without co-cure imperfections
σ_{cc}	Co-cure compressive strength of facesheet
$\sigma_{cr}^{rc\,f}$	Rigid-core critical facesheet stress, defined by Eq. (6)
σ_U	Facesheet lamina strength
σ_{11}	Core crush strength
σ_{13}	Core transverse shear strength in longitudinal (ribbon) direction

Abstract

It has long been established in the literature that the buckling response of thin-shell structures can be very sensitive to the presence of small geometric and loading imperfections. The Shell Buckling Knockdown Factor Project (SBKF) was established by the NASA Engineering and Safety Center (NESC) to develop analysis-based shell buckling design recommendations for stiffened-metallic and composite launch-vehicle shell structures. Large-scale buckling tests were used to validate the modeling and analysis methods applied in developing these analysis-based recommendations. Herein, the test article design methodology for 8-ft-diameter, honeycomb-core sandwich composite cylinder validation tests is discussed and cylinder designs are presented. In this methodology, first, the sandwich composite design space was defined using several nondimensional parameters, and the desired test article design space was determined by examining the designs of launch-vehicle cylinder structures. Essentially all test article designs within certain design parameters were generated and then downselected based on simple closed-form failure calculations and the nondimensional design-space parameters. Four of these designs that spanned a significant portion of the design space of interest and had global buckling as the first predicted failure mode were selected and subjected to higher-fidelity finite element analyses (FEAs): shell-element-based analyses, axisymmetric-element-based analyses, and global-local analyses. The analysis flow discussed in this report supported the design objective. As the analysis flow progressed, designs were downselected so the fidelity of the analysis methods, and consequently their computational cost and accuracy, was increased. The selection of the FEA types created an analysis framework where particular methods complemented each other and reduced the uncertainty of the predicted test article responses. The analysis results are illustrated using several designs when the computationally expeditious closed-form analysis stage is discussed. Once this stage is complete, the higher-fidelity FEA types are illustrated using one selected detailed test article design. Both perfect and imperfect test article geometries were considered.

1.0 Introduction

The NASA Engineering and Safety Center (NESC) established the Shell Buckling Knockdown Factor Project (SBKF) to aid in development of new analysis-based buckling design guidelines for selected classes of metallic and composite launch-vehicle cylindrical shells.[1] Because these new analysis-based buckling design guidelines can potentially be applicable to the next generation of launch vehicles of NASA,[2,3] sandwich composite cylinders were considered by SBKF. For sandwich composite cylindrical shell structures operating primarily under compressive loads, buckling can be a major design consideration, and the critical buckling load is not only influenced by the nominal design, but also by geometric imperfections due to the manufacturing process.[4] Analysis-based design guidelines must, therefore, rely on an analysis methodology that accounts for the presence of manufacturing imperfections and that is validated through large-scale cylinder buckling tests. The developed design and analysis procedure focused on large-scale buckling-

critical sandwich test cylinders representative of flight-like launch-vehicle cylinders. The large-scale testing was planned for a special-purpose test facility at the NASA Marshall Space Flight Center (MSFC), so further design constraints that were related to the test facility capabilities such as the size of a test article that could be accommodated and the maximum load that could be applied needed to be considered.

The contents of this Technical Memorandum will document the analytical methods used to design and analyze large-scale buckling-critical test articles such as composite honeycomb sandwich cylinders. The effort to develop scaled test article designs was accomplished using a practical engineering approach. A series of analysis methods of varying levels of complexity were utilized in the design process to interrogate different potential test article failure modes. Initially, closed-form analyses were used for preliminary design. Several designs that enveloped a large portion of the design space of interest were selected and subsequently subjected to the higher-fidelity finite element analyses (FEAs). Three types of the FEA were considered in the effort: (1) shell-element-based analyses, (2) axisymmetric-element-based analyses, and (3) global-local analyses. Since no single analysis type was able to address all the failure modes of interest, the presented analyses complement each other. A high-level summary of the interrogated failure modes, and advantages and limitations of particular analysis methods are shown in Figure 1. The overall design procedure flow is outlined in Figure 2. Steps other than closed-form or FEAs, such as determination of the design space of interest, test facility constraints, test article manufacturability, and candidate design downselections, are included in the flowchart. Each set of two side-by-side fields connected with a horizontal arrow reflects a procedure action or analysis type and its outcomes. The detailed discussion of steps is provided in Section 2.

In this document, the test-facility design constraints are determined and presented first. Next, a set of nondimensional design parameters describing cylinder design are defined and the design space of interest is determined based on these parameters. Subsequently, a closed-form analysis approach is discussed and used for the preliminary design of buckling-critical sandwich composite cylindrical test articles with four designs being selected that span a significant portion of the desired design space. The description of higher-fidelity finite element models (FEMs) developed and analyzed in order to reduce the predicted response uncertainty and refine the detailed designs are presented next. The considered FEMs include variants with the perfect (nominal) and imperfect (as-measured) geometric configurations of the sandwich cylinders. FEMs of the test article alone and of the test article mounted in the test facility are considered. These models are described and representative analysis results are presented. Finally, concluding remarks are provided.

Analysis Type	Failures Interrogated	Advantages	Limitations
Closed-form	➢ Linear global buckling ➢ Facesheet wrinkling ➢ Facesheet dimpling ➢ Shear crimping	➢ Quickly assess many designs ➢ Calculate otherwise difficult-to-predict failure loads characteristic to the core-scale behavior (core not treated in the homogenized fashion)	➢ Linear solution only (membrane strain component only) ➢ Perfect geometry only ➢ Idealized boundary conditions (no pad-ups or load introduction fixtures)

Shell FEA	➢ Global buckling
	➢ Facesheet strength failures
	  - Axial strain-based
	  - Tsai-Hill failure index-based
		➢ Linear or nonlinear analyses
		➢ Can include measured geometric imperfections
		  - Radial (midsurface)
		  - Thickness
			➢ Cannot capture core crush or shear failures
			➢ Cannot capture core-to-facesheet interface stresses
			➢ Cannot capture end conditions in great detail

Axisymmetric FEA	➢ Global buckling ➢ Homogenized-core strength failures (crush, shear) ➢ Core-to-facesheet interface stresses ➢ Facesheet strength failures	➢ Linear or nonlinear analyses ➢ Interrogate facesheet and core response in detail (high mesh density) at low computational cost ➢ Investigate effects of various end conditions	➢ May not capture minimum buckling mode (if the minimum buckling mode is not axially symmetric) ➢ Cannot include realistic geometric imperfections ➢ Homogenized-core assumption
Global-Local FEA	➢ Global buckling ➢ Homogenized-core strength failures (crush, shear) ➢ Core-to-facesheet interface stresses ➢ Facesheet strength failures	➢ Linear and nonlinear analysis ➢ Interrogate the effects of non-axisymmetric imperfections and/or deformations on core failures (crush, shear) and core-to-facesheet interface stresses ➢ Can model composite layup with higher fidelity than the FEA shell model ➢ Reasonably computationally efficient	➢ Rationale for selecting the local domain(s) ➢ Homogenized-core assumption ➢ Results may not be accurate near edges of local model

Figure 1. Analysis tool: interrogated failure modes, advantages, and limitations.
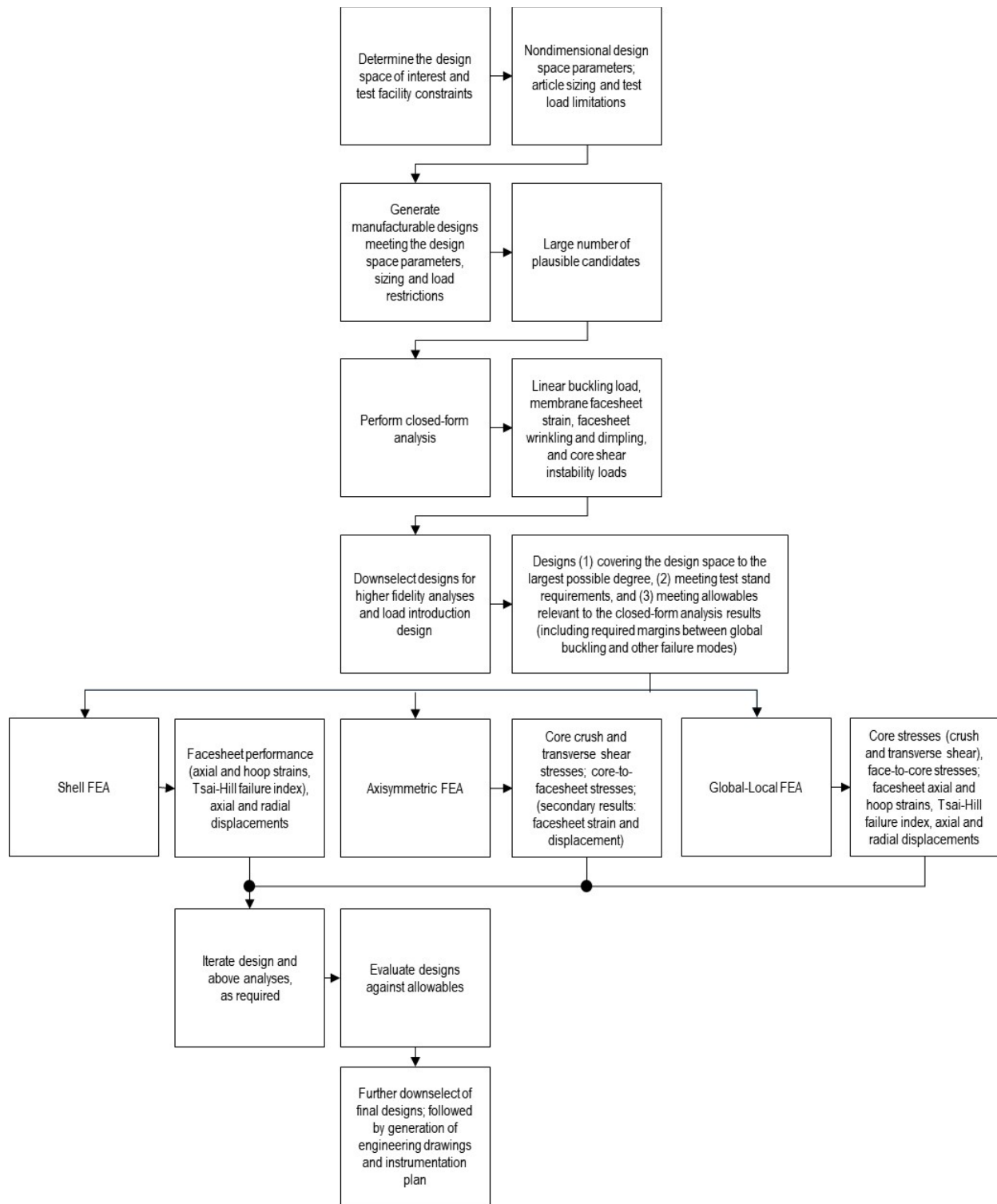
Figure 2. Design and analysis procedure flowchart.

2.0 Test Article Preliminary Design and Analysis

The preliminary design and analysis of the test articles utilized classical lamination theory,[5] with the sandwich core considered as a ply, and used closed-form buckling and strength calculations.[4,6] The considered facesheets were balanced, and either symmetric or unsymmetric. However, all of the facesheets were symmetric about the core, so all of the considered sandwich cylinder walls were balanced and symmetric. Therefore, the laminate stiffness matrix (*ABD* matrix) of the sandwich shells was simplified because the membrane and bending responses were decoupled, and the extension-shear membrane stiffnesses, A_{16} and A_{26}, were identically zero. Additionally, for such sandwich composites with relatively thick cores and thin facesheets, the bend-twist bending stiffnesses, D_{16} and D_{26}, were quite small and were ignored during the closed-form preliminary design analysis.

The test facility is introduced first since the test capability established size and loading constraints for the test articles. The design space of interest was determined next, followed by the closed-form failure predictions, and the resulting downselected preliminary designs.

2.1   Test-Facility Constraints

The challenge in sizing subscale specimens was finding manufacturable test article designs that were representative of present and future launch-vehicle structures and would fail in global buckling before any other structural failure. Due to physical limitations of the test facility at MSFC and programmatic constraints, the SBKF composite effort relied on the testing of subscale, rather than full-scale (up to 27.5-ft diameter), structures. Thus, the test facility restrictions became a design constraint for the test articles. The experimental setup with a sandwich composite cylinder installed is shown in Figure 3. The test facility was designed to test 8-ft-diameter cylinders with lengths up to 10 ft.[7] However, the length chosen for the SBKF composite test articles was 100 in. (8.33 ft). The test facility was rated to apply uniform compression up to 1.5×10^6 lbf or combined compression and bending loads. As shown in Figure 3, the test articles were mounted via aluminum attachment rings to the green-colored metallic stiff load-introduction cylinders. The top and bottom strut structures (orange beams) and load spiders (blue beams), were connected by eight individually controlled and equally spaced hydraulic load lines (white). Different length test articles could be accommodated in the test facility by changing the lengths of the rods in the load lines. The attachment rings feature grooves wider than the end-section thickness of the cylinder walls, allowing the test article to rest on the bottom surface of this groove. The remaining space in the groove was filled with an epoxy grout after a release agent was applied to the inner surfaces of the attachment ring and the end outer surfaces of cylinder wall. This mounting procedure approximated a sliding clamped boundary condition by avoiding bonding of the attachment rings to the cylinder. In past testing with the attachment rings bonded to the cylinder, failure of this bond occurred during test article loading.[8] While the final condition of complete disbonding was not a concern, a transient condition when the bond was failing in a progressive fashion during the load application was determined disadvantageous as it contaminated the test data with nonaxisymmetric response states. In addition, metallic bolts, spaced every 20°, were installed around the circumference of both top and bottom load introduction rings. The bolts were positioned in the radial direction such that they passed through both walls of the metallic load introduction ring, the sandwich wall of the cylinder, and the epoxy grout between the ring walls and the sandwich wall. The holes in the sandwich wall were oversized such that the bolts were not bearing on the sandwich

cylinder during testing. Effectively, the bolts passing through the oversized holes in the sandwich cylinder created a safety feature that would prevent large sections of the test article from liberating from the load introduction rings in case a catastrophic failure and during tear down of the test setup.
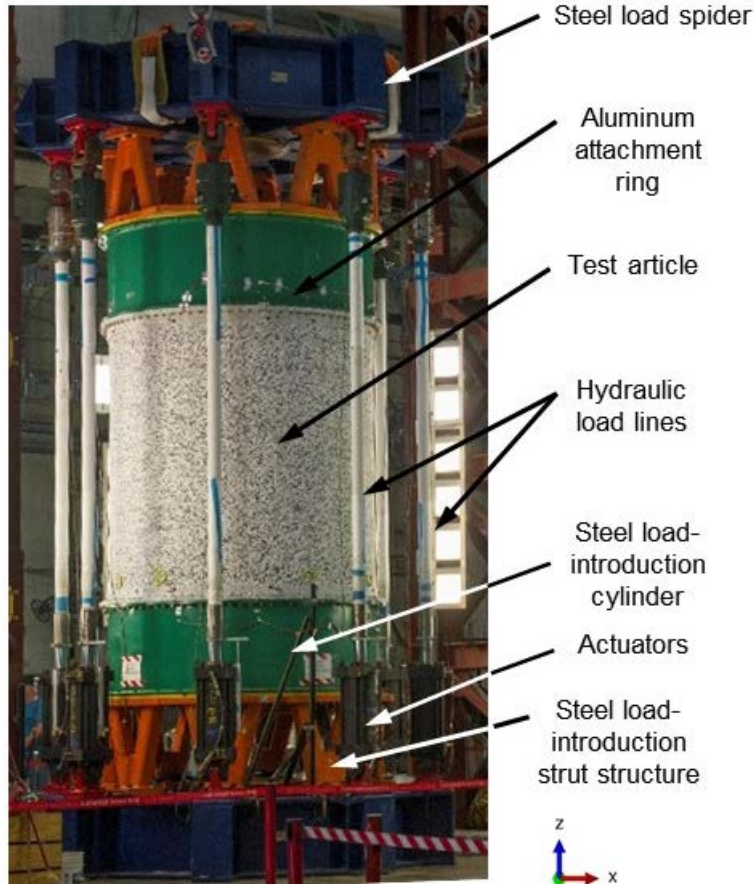
Figure 3. Test facility with a large-scale sandwich composite cylinder installed for testing.

In summary, the subscale sandwich cylinders designed in the present effort were considered to be large-scale (approximately 29% scale as compared to the Space Launch System Core Stage)[9] and were approximately 8.33-ft tall with an 8-ft diameter.

2.2   Test Article Design Space

To determine the design space, several nondimensional design parameters were used to establish guidance in assessing similarity of test article designs to full-scale structures of interest. These nondimensional parameters were a combination of nondimensional geometric and nondimensional sandwich stiffness ratios.

2.2.1   Nondimensional Geometric Parameters

The geometric parameters were considered first. For isotropic cylinders, the R/t ratio, where R is the shell midsurface radius and t is the shell thickness, has long been used as a measure of the thinness of the shell and was an important parameter for determining the buckling imperfection sensitivity.[10] However, for orthotropic stiffened or multilayer shells, the thickness was replaced by

the mean of the stiffness-weighted radii of gyration, which was used as an effective thickness, t_{eff},

$$t_{eff} = \sqrt[4]{144 \frac{D_{11} D_{22}}{A_{11} A_{22}}} \tag{1}$$

where D_{11} and D_{22} are the axial and circumferential bending stiffnesses, respectively, and A_{11} and A_{22} are the axial and circumferential membrane stiffnesses, respectively. Therefore, R/t_{eff} was used in this study as a measure of the thinness of the considered cylinders.

The ratio L/D, where L is the test article length and D is the diameter, was considered as a second geometric parameter as this ratio could influence the buckling response of thin cylinders.

2.2.2 Nondimensional Stiffness Parameters

The relative membrane and bending stiffness ratios have been known to affect the buckling response of cylindrical shells, so several nondimensional parameters were used to assess the shell designs. The first parameters were the ratios of the axial-to-circumferential membrane and bending stiffnesses, A_{11}/A_{22} and D_{11}/D_{22}, which were used as a measure of layup tailoring. These parameters are greater than unity for axially stiff cylinders, less than unity for circumferentially stiff cylinders, and equal to unity for isotropic shells. However, for quasi-isotropic sandwich shells A_{11}/A_{22} is unity and D_{11}/D_{22} is near unity.

The in-plane shear and twisting stiffnesses, A_{66} and D_{66}, respectively, can vary greatly for laminated composite shells. For example, A_{66} and D_{66} are considerably greater for a quasi-isotropic shell than for a specific orthotropic shell with only axial and circumferential plies. Therefore, the nondimensional stiffness parameters,

$$\frac{A_{66}^2}{A_{11} A_{22}} \tag{2}$$

and

$$\frac{D_{66}^2}{D_{11} D_{22}} \tag{3}$$

were considered as measures of the relative in-plane-shear and twisting stiffnesses, respectively. For reference, these parameters are approximately equal to 0.12 for isotropic materials with Poisson's ratio, ν, of 0.3, and for sandwich shells with quasi-isotropic facesheets. Sandwich shells with cross-ply facesheets have values less than 0.12.

For the class of sandwich structures considered, ratios of membrane stiffnesses and analogous ratios of bending stiffnesses were very similar. With this similarity, and because the buckling response was largely dependent on the bending stiffnesses, results for the membrane stiffness parameters are omitted from the discussion for brevity.

2.3 Sandwich Composite Failure Predictions

Classical closed-form equations were used to interrogate the most relevant honeycomb-core sandwich composite failure modes. Specifically, the global buckling load, axial membrane strain at buckling, facesheet wrinkling, facesheet dimpling, and core crimping loads were calculated. The

global buckling equation of Reese and Bert,[6] which considers transverse shear compliance in the core but neglects the in-plane core stiffness, was used to calculate the global buckling load, P_{cr},

$$P_{cr} = 4\pi\, R\, t_f\, \phi\, \sigma_{cr}^{rc} \left(1 - \frac{1}{2}\frac{\phi\, \sigma_{cr}^{rc\,f}\, t_f\, t_c}{G_{xz}\, h^2}\right) \tag{4}$$

where t_f is the facesheet thickness, t_c is the core thickness, h is the distance between facesheet midsurfaces, and G_{xz} is the core transverse shear modulus in the axial-transverse plane. The parameter ϕ is given by

$$\phi = \text{Minimum: } 1 \text{ or } \sqrt{\frac{2G_{xz}\left(1+\sqrt{\bar{v}_{xy}\,\bar{v}_{yx}}\right)}{\sqrt{\bar{E}_x\,\bar{E}_y}}}, \tag{5}$$

and the parameter σ_{cr}^{rc}, the rigid-core facesheet stress, is given by

$$\sigma_{cr}^{rc\,f} = \frac{h}{R}\sqrt{\frac{\bar{E}_x\,\bar{E}_y}{1-\bar{v}_{xy}\,\bar{v}_{yx}}}. \tag{6}$$

The variables $\bar{v}_{xy}$ and $\bar{v}_{yx}$ are the effective facesheet in-plane Poisson's ratios, and $\bar{E}_x$ and $\bar{E}_y$ are the effective facesheet extensional moduli in the axial and circumferential directions. The effective Poisson's ratios and extensional moduli were calculated with the assumption that the facesheets were balanced and symmetric, even though not all considered facesheets were symmetric, and are given by[5]

$$\bar{E}_x = \frac{A_{11}^f\, A_{22}^f - A_{12}^{f\,2}}{A_{22}^f\, t_f} \tag{7a}$$

$$\bar{E}_y = \frac{A_{11}^f\, A_{22}^f - A_{12}^{f\,2}}{A_{11}^f\, t_f} \tag{7b}$$

$$\bar{v}_{xy} = \frac{A_{12}^f}{A_{22}^f} \tag{7c}$$

$$\bar{v}_{yx} = \frac{A_{12}^f}{A_{11}^f} \tag{7d}$$

where the A_{ij}^f are the facesheet membrane stiffnesses. Using these simplified effective properties was reasonable for the case of this buckling prediction because the sandwich shell itself was balanced and symmetric.

The axial membrane strain at buckling, ε_{cr}, was calculated based on P_{cr}, the cylinder axial stiffness, and the assumption that all the load was carried by the facesheets

$$\varepsilon_{cr} = \frac{P_{cr}}{4\pi\, R\, t_f\, \bar{E}_x}. \tag{8}$$

The facesheet wrinkling, facesheet dimpling, and core crimping failure loads were calculated based on equations given by Vinson for honeycomb-core sandwich panels[4] and assuming pure

compression loading of the cylinders. As such, the facesheet wrinkling load, P_{FW}, was calculated as

$$P_{FW} = 4\pi R t_f \sqrt{\frac{2}{3}\frac{t_f}{t_c}\frac{E_c\sqrt{\bar{E}_x\bar{E}_y}}{1-\bar{v}_{xy}\bar{v}_{yx}}} \tag{9}$$

where E_c is the effective core transverse shear modulus. The facesheet dimpling load, P_{FD}, was calculated as

$$P_{FD} = 4\pi R t_f \frac{2\sqrt{\bar{E}_x\bar{E}_y}}{1-\bar{v}_{xy}\bar{v}_{yx}}\left(\frac{t_f}{d}\right)^2 \tag{10}$$

where d is the honeycomb-core cell size. Finally, the core-shear-instability load, P_{CS}, was calculated as

$$P_{CS} = 4\pi R t_f \frac{G_{xz}t_c}{2t_f}. \tag{11}$$

It should be noted that Eq. (11) is simplified for very thin facesheets. This simplified version was used herein because it predicted more conservative loads than a corresponding equation without this simplification (similar to the equation given in Reference 6 for core shear buckling in terms of facesheet stress). It was more difficult to justify using the simplified effective properties in the equations for P_{FW} and P_{FD} than it was for P_{cr} because these calculations were meant to predict the performance of the individual facesheets. However, the main objective of this initial design study was to have all other predicted failure loads be 1.4 times higher than the predicted global buckling load to provide reasonable separation between failure modes, and these equations could be used in this capacity. As shown later, the calculated P_{FW} and P_{FD} for all the selected designs were quite high—between five and 80 times P_{cr}. Additionally, four of the five selected designs had symmetric facesheets that satisfied the assumptions, and the fifth design had relatively low membrane-bending coupling that approximated this assumption.

2.4 Closed-Form Test Article Design and Limitations

The first step in designing the test articles was to determine the design space of interest by calculating the nondimensional geometric and stiffness parameters for available launch-vehicle cylindrical-shell designs. These designs were a combination of available real, proposed, and SBKF-generated launch-vehicle designs. The nondimensional launch vehicle geometry parameters are shown as the green squares in Figure 4 with values of L/D that vary from 0.16 to 1.7, and with values of R/t_{eff} that vary from 52 to 121. The low values of L/D represent short cylinders such as skirts, and the higher values represent relatively long cylinders such as interstages. The launch vehicle nondimensional bending stiffness parameters are shown in Figures 5 and 6 versus R/t_{eff}. Most of the launch-vehicle D_{11}/D_{22} ratios are between one and two, but two proposed designs are highly tailored with $D_{11}/D_{22} > 2$, as shown in Figure 5. Most of the considered launch-vehicle $D_{66}^2/D_{11}D_{22}$ ratios vary between 0.024 and 0.16, but within this group, the majority of these ratios are less than the quasi-isotropic sandwich value of approximately 0.12, as shown in Figure 6.
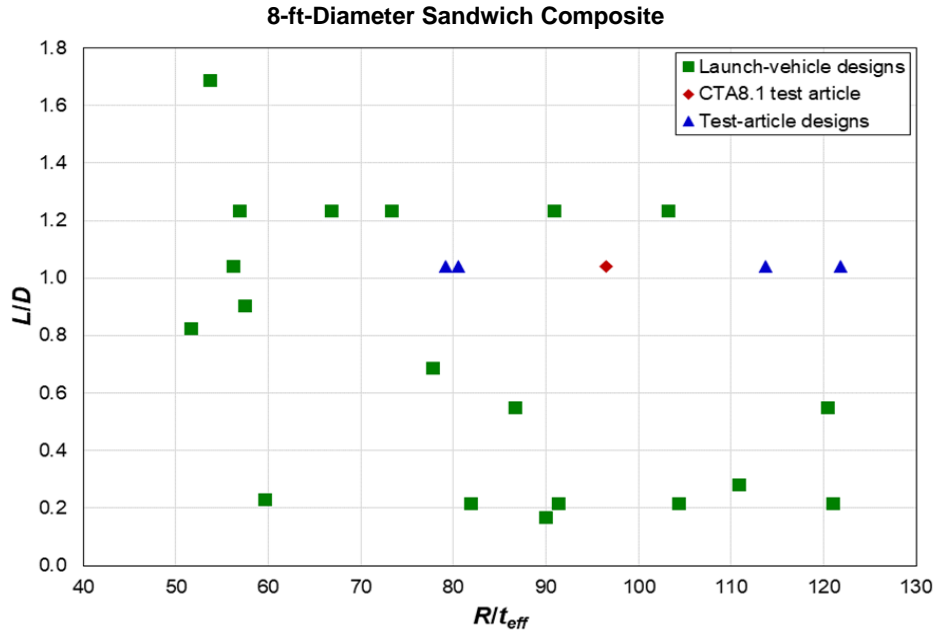
Figure 4. Launch vehicle and test article nondimensional geometric parameter L/D versus R/t_{eff}.
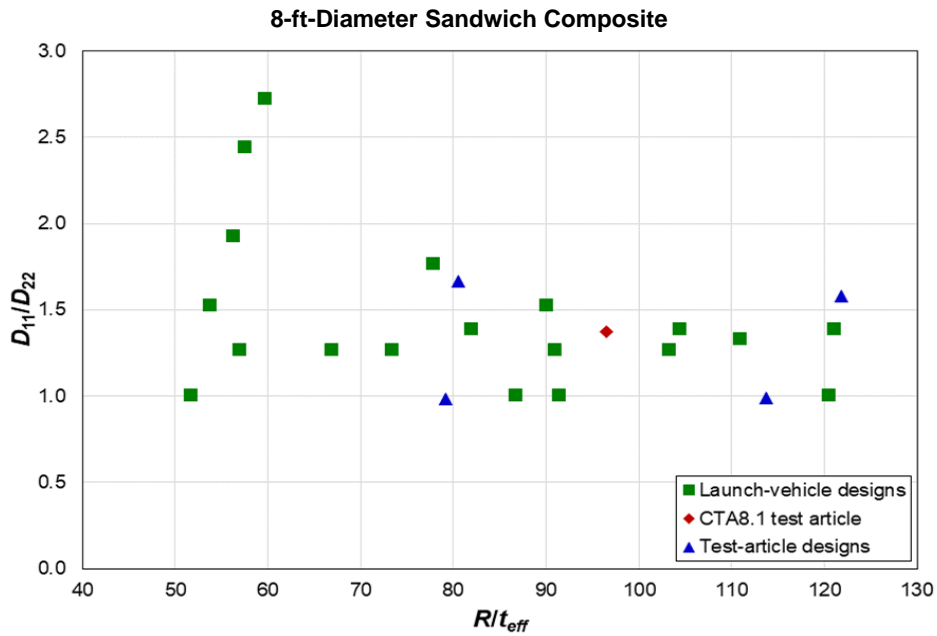
Figure 5: Launch vehicle and test article nondimensional bending stiffness parameter D_{11}/D_{22} versus R/t_{eff}.
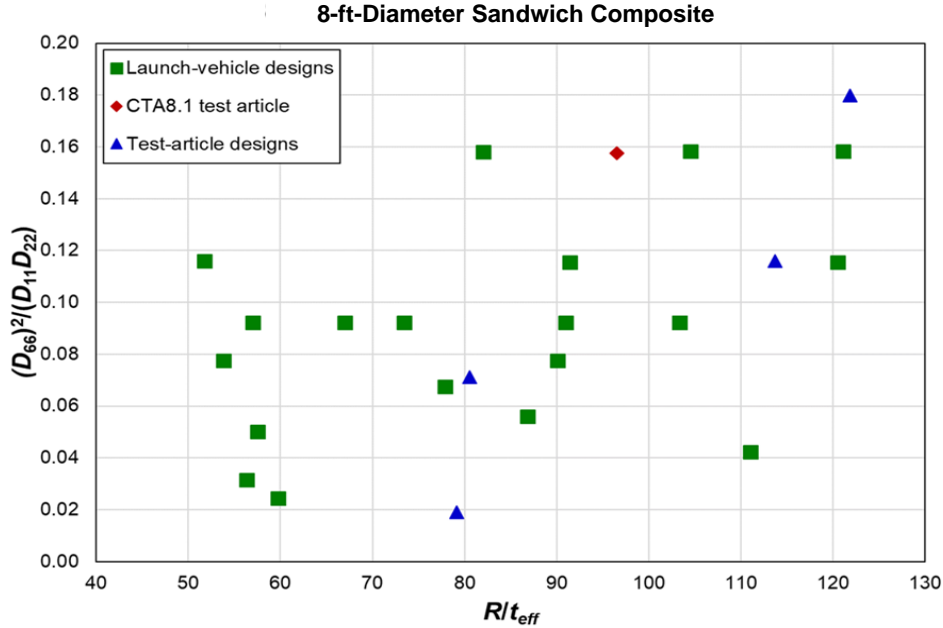
Figure 6. Launch vehicle and test article nondimensional bending stiffness parameter $(D_{66})^2/(D_{11}D_{22})$ versus R/t_{eff}.

The next step in designing the test articles was to generate designs, calculate the nondimensional geometry and stiffness parameters, and use Eqs. 4 and 8–11 to determine the relevant sandwich-structure failure loads. These calculations were made using an SBKF-developed computer code to calculate essentially all potential designs for a given set of parameters. Specifically, the facesheets considered were between two and twelve 0.0054-in.-thick plies of Hexcel IM7/8552-1 carbon/epoxy (145 g/m^2 fiber areal weight (FAW), traditionally provided in the SI units). Potential ply angles were limited to 0°, 90°, ±30°, ±45°, and ±60°. Hexcel aluminum honeycomb core made of 5056 aluminum alloy with 1/8-in. cells, 0.007-in. cell wall thickness, and a volumetric density of 3.1 pounds per cubic foot (pcf) was selected with thicknesses between 0.1 in. and 0.5 in. at increments of 0.05 in. Additionally, facesheets were constrained to be balanced by grouping the ±30°, ±45°, and ±60° plies. Designs with $P_{cr} > 2.0 \times 10^6$ lbf, $\varepsilon_{cr} > 10,000$ µε, and $P_{FW}, P_{FD}, P_{CS} < 1.4 P_{cr}$ were rejected. This procedure resulted in nearly 100,000 individual designs for further investigation. The number of designs was further reduced by eliminating designs that had no off-axis (angle) plies, had $P_{cr} > 1.5 \times 10^6$ lbf, or had $\varepsilon_{cr} > 5000$ µε; this reduction resulted in approximately 1700 individual designs. The condition that $\varepsilon_{cr} \leq 5000$ µε for the accepted designs may seem very conservative, but the ε_{cr} calculation considered only membrane strain, therefore, the strains at buckling in test articles derived from these designs were expected be significantly higher. Finally, designs were downselected by choosing designs that had nondimensional design parameters that bounded as much of the desired launch vehicle design space as possible. Four 8-ft-diameter sandwich composite test article (CTA8.x) designs, listed in Table 1, were selected for further examination. Soon after the designs were selected, a thicker ply material was chosen for CTA8.2B due to material availability. The corresponding closed-form failure predictions for these designs for each potential failure mode are shown in Table 2. These results show that for all selected configurations, the lowest failure prediction was associated with global buckling.

Table 1. Closed-form designs.

Design	Facesheet layup	Core thickness, in.	Ply thickness, in.	Fiber aerial weight (FAW),[*] g/m^2
CTA8.1	$[\pm 45/0/\overline{90}]_s$	0.25	0.0052	n/a
CTA8.2B	$[\pm 60/0]_s$	0.20	0.00694	190
CTA8.3	$[\pm 30/\overline{90}]_s$	0.20	0.0054	145
CTA8.4	$[\pm 30/90/0]_s$	0.30	0.0054	145
CTA8.5	$[90/0/90/0/\mp 30/90/90/0]_T$	0.30	0.0054	145

[*]Even though this paper uses the English units, it is customary to express FAW in the International System of Units (SI).

Table 2. Sandwich composite failure predictions.

Design	P_{cr}, lbf	P_{FW}, lbf	P_{FD}, lbf	P_{CS}, lbf	ε_{cr}, με
CTA8.1	0.999 x10^6	6.31 x10^6	32.6 x10^6	3.39 x10^6	5170
CTA8.2B	0.973 x10^6	1.75 x10^6	12.2 x10^6	2.71 x10^6	4959
CTA8.3	0.541 x10^6	1.09 x10^6	4.81 x10^6	2.71 x10^6	3902
CTA8.4	1.27 x10^6	2.37 x10^6	33.8 x10^6	4.07 x10^6	4454
CTA8.5	1.15 x10^6	3.80 x10^6	77.2 x10^6	4.07 x10^6	3917

A test article designated CTA8.1 was the first sandwich composite cylinder tested under the composite part of the SBKF program. This cylinder was designed prior to the present effort using a slightly different approach and fabricated by Northrop Grumman under a cooperative agreement.[8] The nondimensional parameters of CTA8.1 are shown with red diamonds and of CTA8.2B through CTA8.5 are shown with blue triangles in Figures 4, 5, and 6. Consider first the nondimensional geometric parameters in Figure 4. Though the considered launch-vehicle L/D ratio spanned a range from quite short to relatively long, a single intermediate value was chosen for the test articles due to the limited number of designs to be manufactured. These test articles spanned a significant portion of, but not the entire, launch-vehicle R/t_{eff} design space under consideration. The difficulty in designing the subscale test articles with a low R/t_{eff} ratio resulted from their tendency to have buckling loads higher than the test-facility load rating, or to reach the compressive material strength limit before buckling. While the latter situation could be desirable for actual designs, such test article designs would not allow the required experimental interrogation of the buckling response. Additional limitations were encountered when designing subscale sandwich composite test articles with the high R/t_{eff} ratios due to manufacturing difficulties in producing sandwich composite structures with very thin cores, especially with honeycomb cores.

The nondimensional stiffness parameters are shown in Figures 5 and 6. The data in Figure 5 indicates that three of the test article designs were axially stiff (CTA8.1, CTA8.3, and CTA8.4), two had essentially equal axial and circumferential stiffnesses (CTA8.2B and CTA8.5), and that these spanned a significant portion of the launch-vehicle design space. The data in Figure 6 indicates that the considered test article designs spanned the entire presented launch-vehicle design space for $D_{66}^2/D_{11}D_{22}$.

3.0 Detailed Cylinder Design and Finite Element Modeling

The closed-form calculations used for the initial test article design had known inherent limitations. The predicted buckling was a linear solution and the corresponding strains were limited to the membrane component only. From a practical engineering standpoint, the analysis was limited to a general sandwich cross section that could not be used in designing load-introduction features such as the attachment rings or pad-ups (end thickness buildups), or considering geometric imperfections. Therefore, a more-detailed, higher fidelity design and analysis using the FEM was undertaken.

While in the previous section all five designs were discussed to address populating the design space of interest, in this section, the detailed design and analysis of only the CTA8.3 test article is presented as a representative illustration of the design and the analysis procedure used for all of the remaining test articles (brief summaries of the results for the remaining configurations are presented in Appendices A through C for CTA8.2B, CTA8.4, and CTA8.5, respectively). The FEMs developed to support the detailed design and analysis effort are introduced in this section.

3.1 Detailed Cylinder Design

The test articles, CTA8.2B, CTA8.3, CTA8.4, and CTA8.5, were designed to be manufactured in the MSFC Composite Technology Center using automated fiber placement laying 0.5-in.-wide unidirectional tows and autoclave cure. The CTA8.3 acreage design had two axially stiff $[\pm30/\overline{90}]_s$ facesheets separated by a 0.20-in.-thick aluminum honeycomb core. This design resulted in a relatively thin (R/t_{eff} of 122), axially stiff ($D_{11}/D_{22} \approx 1.5$) test article. The high R/t_{eff} ratio was a result of the thin core, and the large axial-to-circumferential bending stiffness ratio was achieved by using two pairs of $\pm30°$ plies and only one $90°$ ply in each facesheet.

The detailed CTA8.3 design included pad-ups in the facesheets and a higher density core at the cylinder ends to mitigate some of the high bending strains in the facesheets and high crush and shear stresses in the core associated with the load introduction. The pad-ups included up to four plies of the same Hexcel IM7/8552-1 tape used in the acreage facesheets: two $+45°$ plies and two $-45°$ plies that were interleaved with the acreage plies. The inner mold line (IML) facesheet layups in the pad-up regions are shown in Table 3 where pad-up plies are listed in bold font. The outer mold line (OML) facesheets were symmetric with the IML pad-ups. The thickness of the pad-up layers was built up away from the IML of the cylinder for both inner and outer facesheets because the cylinder was manufactured on a constant-diameter tool. The transition from the 8.1-pcf core to the 3.1-pcf core, also shown in Table 3, occurred 10 in. from the cylinder ends, i.e. away from the pad-up ply terminations, to prevent interactions between core splices and pad-up ply terminations. Where the core sections were spliced, a width of approximately 0.25 in. (0.125 in. to both sides of the splice) was filled with an epoxy grout Hysol EA9396.6MD.

Table 3. Core transition and layups in acreage and pad-up regions.

CTA8.3 cylinder sections measured from cylinder ends, in.	Core Density, pcf	IML facesheet layup, degrees
Greater than 20 (Acreage)	3.1	[30/-30/90/-30/30]
18 to 20	3.1	[30/-30/**45**/90/-30/30]
16 to 18	3.1	[30/-30/**45**/90/-30/**-45**/30]
14 to 16	3.1	[30/-30/**45**/90/**45**/-30/**-45**/30]
10 to 14	3.1	[30/**-45**/-30/**45**/90/**45**/-30/**-45**/30]
0 to 10	8.1	[30/**-45**/-30/**45**/90/**45**/-30/**-45**/30]

*Bold font indicates a pad-up ply.

3.2 Finite Element Modeling

Three types of FEA were considered in the detailed design process: (1) shell-element-based analyses, (2) axisymmetric-element-based analyses, and (3) global-local analyses. Since no single FEA type was able to address all the failure modes of interest, the presented analyses complemented each other rather than presented alternatives. Capabilities and limitations of particular analysis methods, including the interrogated failure modes, were presented in Figure 1. The overall procedure flow was outlined in Figure 2. The three FEA types listed in Figures 1 and 2 constituted the majority of the effort in the detailed design process.

3.2.1 Shell-element-based Model

A shell-element-based model of the composite sandwich cylinder was developed using the commercial general-purpose FEA software Abaqus[11] as the primary higher-fidelity design and analysis tool. The other two FEMs were developed subsequently to mitigate some of the limitations of the shell-element-based analysis.

The initial shell-element-based model for rapid evaluation of the designs included only the sandwich cylinder with the pad-ups and attachment rings, but excluded the test fixture. This model is identified in Figure 7 as a subset of a detailed shell-element-based model that included the test fixture. The test article and attachment rings were modeled using the S4R four-noded reduced-integration shell elements. The sandwich structure was modeled as a layered composite with the individual facesheet plies and the honeycomb core treated as individual layers. Based on mesh convergence studies performed previously for the similar CTA8.1 test article,[3] the mesh size of the composite cylinder was chosen to be 0.5° in the circumferential direction (or approximately 0.4 in.) by 0.5 in. in the axial direction. This model featured approximately 155,000 nodes resulting in approximately 930,000 degrees of freedom. The basic material properties (in-plane extensional stiffnesses E_{11}, E_{22} and in-plane Poisson's ratio ν_{12}) of IM7/8552-1 used in the FEA are shown in Table 4 and were obtained from the SBKF-commissioned testing conducted by a vendor.[12] The lamina strength properties (X_t, X_c, Y_t, Y_c, and S) were sourced from the internal NASA memorandum.[13] The cured ply thickness, t_p, of 0.0054 in. was used for the FAW of the 145 g/m^2 material in the analyses of CTA8.3 through CTA8.5, and 0.00694 in. for the FAW of the 190 g/m^2 material in the analyses of CTA8.2B. The material properties (in-plane extensional stiffnesses E_{11}, E_{22}, in-plane shear stiffness G_{12}, transverse shear stiffnesses G_{13}, G_{23}, transverse crush strength σ_{11}, and axial-transverse shear strength σ_{13}) of the 3.1-pcf and 8.1-pcf aluminum honeycomb core[14] are shown in Table 5.
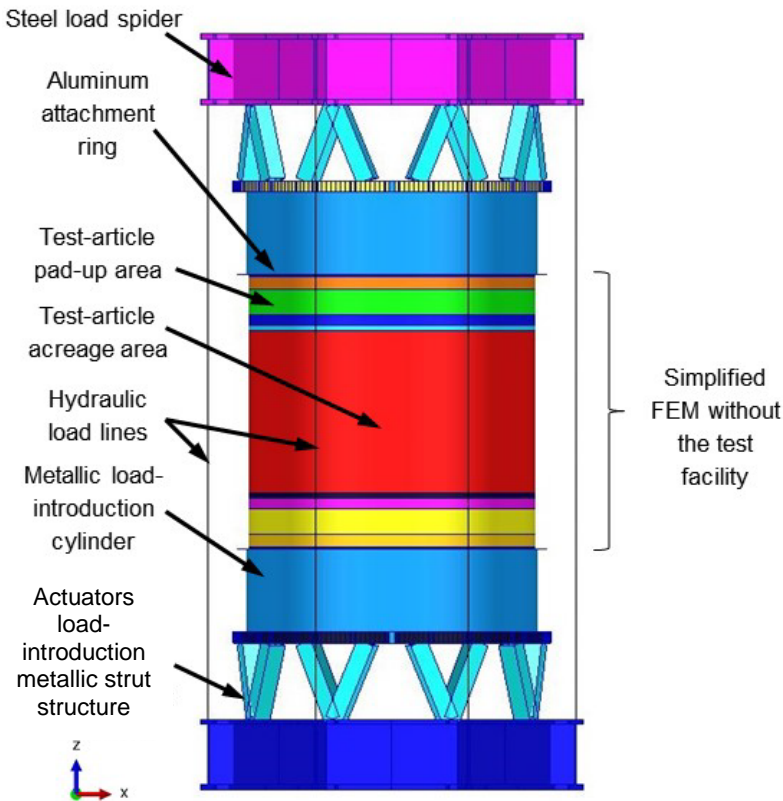
Figure 7. FEM property regions of a composite sandwich test article installed in the test facility.

Table 4. Properties of carbon-epoxy IM7/8552-1 material system.

Property, Unit	E_{11}, Msi	E_{22}, Msi	ν_{12}	t_p, in.
Value	20.4	1.33	0.345	0.0054[*] 0.00694[**]

[*] FAW = 145 g/m^2
[**] FAW = 190 g/m^2

Table 5. Properties of 5056 aluminum honeycomb core.

Property, Unit	Density, pcf	E_{11}, psi	E_{22}, psi	G_{12}, psi	G_{13}, psi	G_{23}, psi	σ_{11}, psi	σ_{13}, psi
Value	3.1	5.8	2.9	1.45	45,000	20,000	350[*] 260[**]	250[*] 200[**]
	8.1	15.66	7.83	3.915	143,000	51,000	1900[*] 1300[**]	945[*] 740[**]

[*] Typical
[**] Minimum

The aluminum attachment ring, shown in Figure 3, was modeled using the same S4R elements as the cylinder sandwich structure. The plane of the S4R elements used to model flanges of the ring was perpendicular to the longitudinal axis of the cylinder. The webs (side walls of the ring forming a groove accommodating the end section of sandwich cylinder) were modeled as innermost and outermost "plies" of the sandwich structure and assigned isotropic aluminum properties. Potting of the sandwich cylinder in the load introduction rings was modeled as potting "plies" in the layered shell elements. These potting "plies" were placed between the innermost IML facesheet

ply and the inner web of the ring, and between the outermost OML facesheet ply and the outer web of the ring. Since a release agent was applied to the ends of the cylinder and inside the groove of the load introduction ring, a sliding contact boundary condition was effectively targeted. To represent this condition without resorting to modeling sliding contact interaction, the actual stiffness of the potting grout was used in the hoop direction ($E_y = 1.10$ Msi) but a stiffness that was three orders of magnitude less was used in the axial direction ($E_x = 1.10$ ksi).

Once the designs were interrogated and deemed satisfactory with the simple shell-element-based analysis, a model incorporating the entire test fixture, as shown in Figure 7, was developed to verify that the structural responses with and without the test fixture were similar providing a reasonable estimate of the expected test behavior including predictions of loads and displacements in the eight load lines. The metallic load-introduction cylinders, shown in Figure 7 as the blue structure, above and below the test article, were modeled using shell elements. These structures were relatively stiff with elements having larger edge sizes of 1.5 in. in the circumferential direction and 2 in. in the axial direction. The load spiders and struts at the very top and bottom of the test setup were modeled with the B31 beam elements with even larger dimensions. The eight vertical load lines were modeled using a single T3D2 truss element for each. The FEM of the cylinder with the entire test setup featured approximately 166,000 nodes resulting in approximately 995,000 degrees of freedom.

Two geometric variations of each shell FEM were developed and analyzed. The first FEM used the nominal dimensions of the test cylinder, is referred to as the perfect model. The second FEM, referred to as the imperfect model, was based on the OML and IML cylinder surface measurements performed using the structured-light geometry measurements[15] of a previously tested similar test article. The imperfect model had two variations of its own. The first variation reduced the geometric imperfections to the midsurface radial imperfection only, termed the radial imperfection model. This radial imperfection was obtained by measuring the IML and OML cylinder surfaces and averaging the two measurements. The second imperfect geometry variation accounted for the presence of both radial and thickness imperfections. The thickness imperfection was obtained by calculating the difference between the OML and IML scans. The radial imperfection shell models had the same connectivity as the perfect model, but with the nodal locations adjusted to reflect the radial imperfections. No effort was undertaken to characterize and account for any potential manufacturing or installation residual strains in the test articles, thus the imperfect models were stress-free before the test load application. The shell model that included both the radial and thickness imperfections used the same set of adjusted nodal locations and additionally included many unique shell property cards to account for thickness variations. It was assumed that the thickness variations of the facesheets were minimal when compared to the thickness variations of the honeycomb core, thus the entire thickness variation was implemented as a core thickness variation only.

Despite the fact that several sandwich test articles are considered herein, the only measured geometry imperfection relevant to the CTA8.2B through CTA8.5 designs that was available during the design and analysis process was the measurement of CTA8.2 shown in Figure 8.[16] The CTA8.2 test article, not described in this document, was nearly identical to CTA8.2B with the exception of the 3.1-pcf core being used throughout the cylinder. The imperfection shown in Figure 8 was measured after the sandwich cylinder was potted in the aluminum load introduction rings. Consequently, the shimming process preceding the potting process also influenced the measured geometric imperfections, especially in the direct proximity of the load introduction rings.

Nevertheless, the resulting imperfections presented in Figure 8 were assumed to correspond to a stress-free condition and no installation preload was applied in analyses. Ultimately, the actual imperfections of a particular design are not known until the test article is manufactured and measured, so any prior analysis had to rely on some assumptions made about the geometric imperfections. Since all the cylinders (CTA8.2 and CTA8.2B through CTA8.5) were designed to be constructed on the same tool and installed (potted) in the same aluminum load introduction rings, it was assumed that the CTA8.2 imperfections were representative of the imperfections of this entire test article family.

(a)

(b)
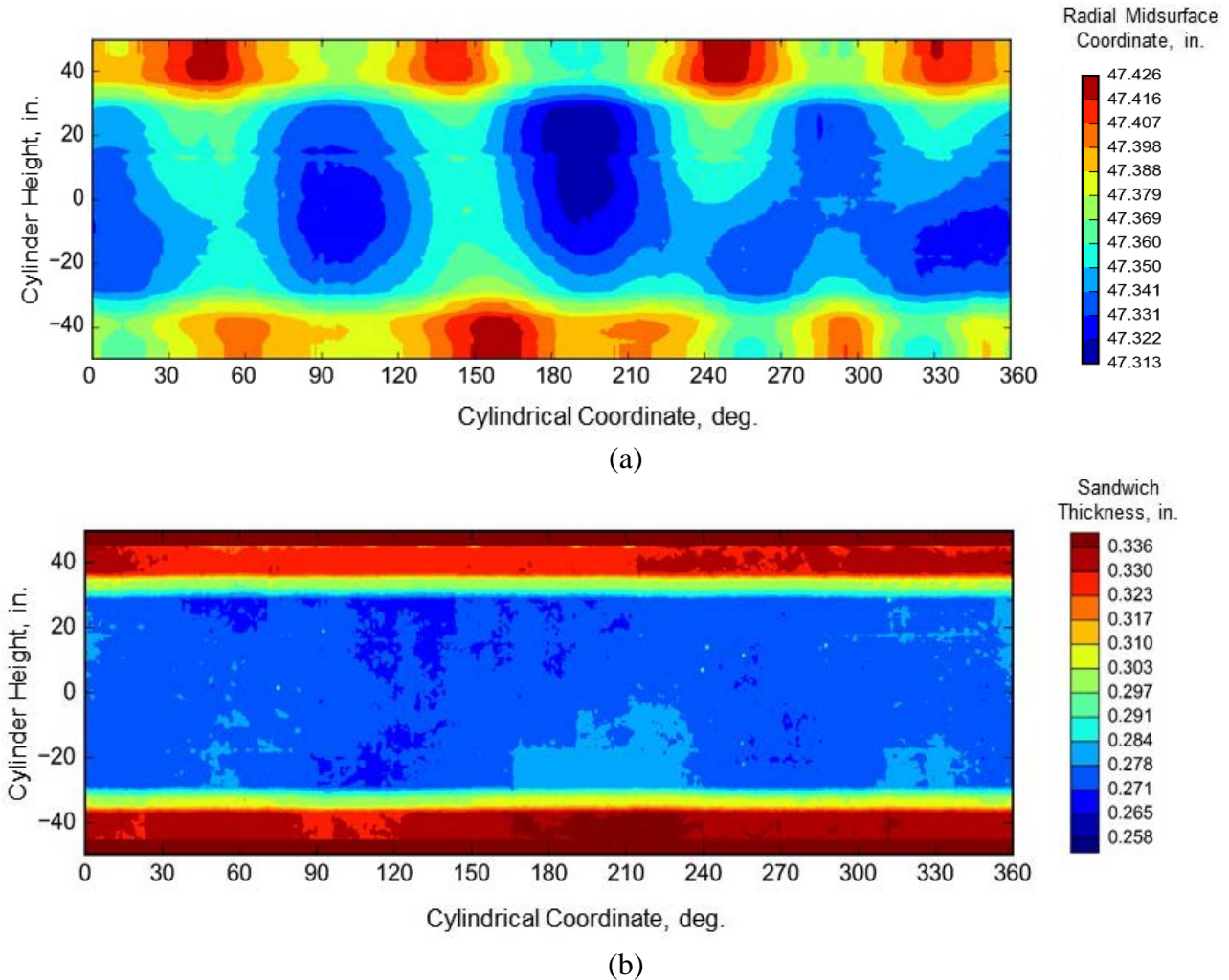
Figure 8. Test article CTA8.2 measured imperfections: (a) midsurface radial and (b) thickness.

The results presented later in this document for the imperfect models include only the radial imperfections for CTA8.3, but both radial and thickness imperfection results are presented for the remaining designs, i.e., CTA8.2B, CTA8.4, and CTA8.5. The radial midsurface imperfections used in the analyses are shown in Figure 8(a) and the thickness imperfections are shown in Figure 8(b). The top and bottom 20 in. of the thickness imperfection map shown in Figure 8(b) accounts for the presence of pad-ups, the detail design feature described in Section 3.1. It is to be noted, however, that the pad-up designs varied slightly among the different cylinder designs, and this section of the reference imperfection map was adjusted to properly account for the number of pad-up plies.

17

3.2.2 Axisymmetric-element-based Model

The axisymmetric-element-based model is shown in Figure 9 and was primarily used to interrogate the core crush and shear strength failures, core-to-facesheet interface stresses, and facesheet strength failures in the prebuckled condition. Abaqus four-noded CAX4 axisymmetric elements were predominantly used to model half of the barrel height, including the sandwich structure faces and core, as well as the load introduction rings and the potting grout. Individual plies were each modeled with one layer of CAX4 elements. The sandwich core, load introduction ring, and potting grout were modeled with multiple CAX4 elements across the thickness (i.e., in the radial direction). The ply drops were modeled as occurring over a distance of twice a ply thickness using CAX4 elements and a small number of three-noded CAX3 axisymmetric elements, as shown in Figure 10a. Using micrographs that became available after the analysis was completed, this ply-drop dimension was found to be unrealistically short. The dimensions of the core-splice-region transition from 8.1-pcf to 3.1-pcf core are shown in Figure 10b. To account for the presence of the core-splice adhesive in this area (neglected in the shell-element-based analysis), the material properties were adjusted. Specifically, for a particular density of the honeycomb core and core-splice adhesive combination, the larger of the two properties were selected as the material property representative of the region (i.e., no rule of mixture was applied). The properties for the combination of the 3.1-pcf and the 8.1-pcf honeycomb core with the core-splice adhesive are shown in Table 6 where ν_{13} and ν_{23} are the axial-transverse and circumferential-transverse Poisson's ratios, respectively.
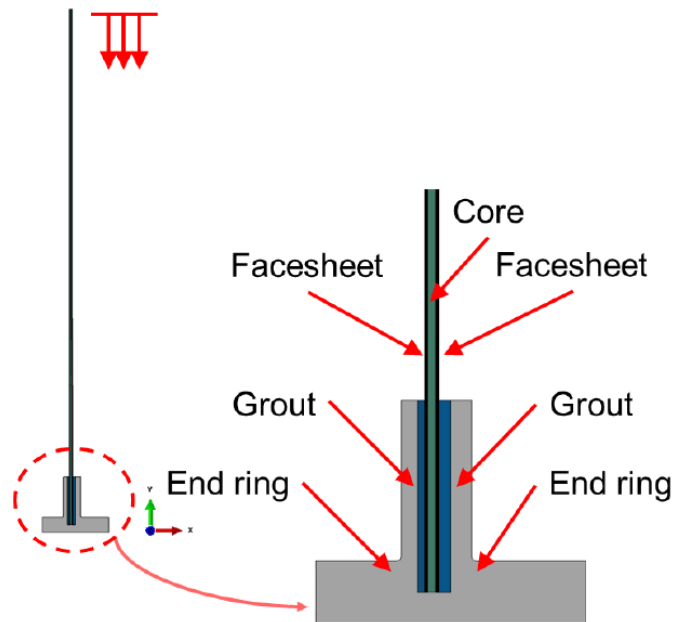
Figure 9. Axisymmetric-element-based model.

(a)   (b)
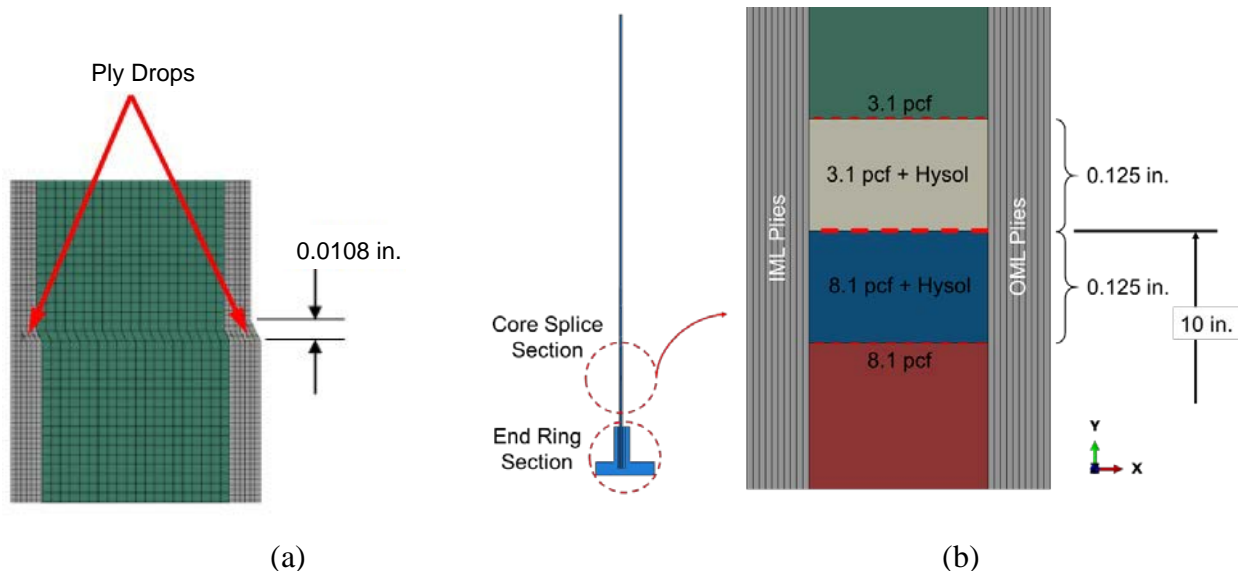
Figure 10. Features of the CTA8.3 axisymmetric-element-based model: (a) ply drop and (b) core splice.

Table 6. Properties of 5056 aluminum honeycomb core with Hysol potting grout.

Property, Unit	E_{11}, Msi	E_{22}, Msi	E_{33}, Msi	ν_{12}	ν_{13}	ν_{23}	G_{12}, Msi	G_{13}, Msi	G_{23}, Msi
Hysol with 3.1 pcf Core	0.290	0.290	0.290	0.2	0.2	0.2	0.143	0.121	0.121
Hysol with 8.1 pcf Core	0.435	0.290	0.290	0.2	0.2	0.2	0.143	0.121	0.121

To improve computational efficiency, only half of the cylinder height was modeled. The bottom of the model was fixed and the midlength location was assigned the symmetrical boundary conditions and an axial compressive load. These end conditions effectively meant that only an odd number of axial halfwaves was allowed in the solution (an even number of halfwaves would require application of the antisymmetric boundary conditions at the midlength location). However, realistic geometric imperfections and buckling modes with circumferential variation also could not be implemented or predicted with the axisymmetric model, so this model was not used for primary assessment of the buckling response. Rather, the axisymmetric model was used to evaluate the core crush and transverse shear stresses up to buckling load because these stresses were not available from the shell-element-based analysis. The largest core stresses were predicted to be in the vicinity of the end rings where there was little circumferential variation, and at the ply drops, which were very localized. Even if the shell model and the axisymmetric model would produce different buckling shapes, the core response metrics obtained slightly below the buckling load from the axisymmetric analysis were still valuable for the assessment of the core at incipient buckling. The axisymmetric analysis was exercised only for a perfect cylinder configuration.

Several variants of the axisymmetric analysis were performed. The main difference between these variants was in how the interaction between the sandwich cylinder wall and the potting grout within the ring groove was modeled. Specifically, that interface was modeled as both sliding contact and fixed (fully bonded) interaction. As discussed in Section 2.1, mold release was applied to the test article and end rings prior to potting to preclude bonding at those interfaces. Therefore,

a sliding contact interaction, i.e., allowing sliding and/or separation between both OML and IML facesheets, and the potting grout was assumed to be the modeling baseline; this variation of the axisymmetric model is referred to as sliding in the remainder of this report, and the sliding interactions were modeled to be frictionless. A sensitivity study with a wide range of friction coefficients showed that, short of completely fixed, there was little influence of friction on the predicted response. Analyses using the Abaqus tie command to fix the surfaces, termed the tied condition, were also performed. This condition was representative of an ineffective application of the mold release to the ends of the test article and the load introduction rings in the potting process.

Beyond the baseline sliding interaction and the tied interaction, another constraint condition variation was the assumption that the OML facesheet surface was tied to the grout in the load introduction ring while the IML facesheet surface had the sliding interaction, i.e., free to slide and/or separate from the grout. This analysis variant is used to simulate the condition where the growing radial expansion of the loaded cylinder at its potted ends resulted in a large surface pressure being exerted by the OML facesheet on the grout. It was envisioned that such a pressure combined with the insufficient application of the release agent could result in the locking of the two surfaces. This variation of the axisymmetric-element-based model is later referred as sliding IML/tied OML. The tied and sliding IML/tied OML model variants were intended to give insight into "the worst-case scenario," i.e., when the cylinder-grout interactions were off-nominal.

The axisymmetric-element-based model included approximately 220,000 elements and 685,000 degrees of freedom. A geometrically nonlinear implicit solver was used to obtain solutions.

3.2.3   Global-local Model

The global-local analysis was primarily used to assess the honeycomb-core performance without some of the limitations of the axisymmetric analysis as stated in Section 3.2.2, namely the inability to incorporate realistic geometric imperfections in the axisymmetric model. For the global-local model, the global part of the analysis was performed on the shell-element-based model, as described in Section 3.2.1. The spatial domain for the local model (or multiple models, if required) were chosen based on what was perceived as a possible core performance-critical location based on the global analysis. This selection constituted possibly the weakest attribute of the approach: while large rates of radial deformation and/or facesheet strain levels might have been a good indication of core critical performance locations, there was no guarantee that such a selection criteria would be a completely reliable selector for the spatial domains to be subjected to the local analysis. The selected spatial domain of the local model for CTA8.3 was quite large and is highlighted in red in Figure 11.

The global-local analysis was accomplished by applying what is referred to in the Abaqus[11] documentation as the node-based submodeling technique. In the submodeling technique, the local region was assumed not to have a major or driving influence on the overall global solution. The practical implication of this limitation for the problem at hand was that the technique was likely only valid in the prebuckled regime because the assumption would be violated if the analysis were extended to the incipient buckling or the postbuckled response, especially if the buckling event originated in the local spatial domain of the model. The local model was constructed using the solid elements (C3D8R) to model the core in a homogenized fashion, and the continuum shell elements (SC8R) to model the facesheets in both acreage and pad-up sections, as shown in the right upper part of Figure 11. The displacements from the global shell-element-based model obtained along the boundaries of the local model constituted the continuity of the two models.

More specifically, the driven (enforced) degrees of freedom in the local model were chosen automatically by Abaqus based on the distance between the driven solid-element node and the midsurface of the shell. If the distance was less than 10% of the maximum shell thickness, all displacement components were driven. For the nodes outside the 10% threshold, only the displacement components parallel to the shell midsurface were driven. In other words, the solid-element nodes outside the 10% thickness threshold were not driven in the direction perpendicular to the surface of the shell. The amount of work performed by the interface nodes of the global domain and by the interface nodes of the local domain was computed and compared to assess the goodness of the interaction of the global and local domains. Only small differences were found and are documented in Appendix D.
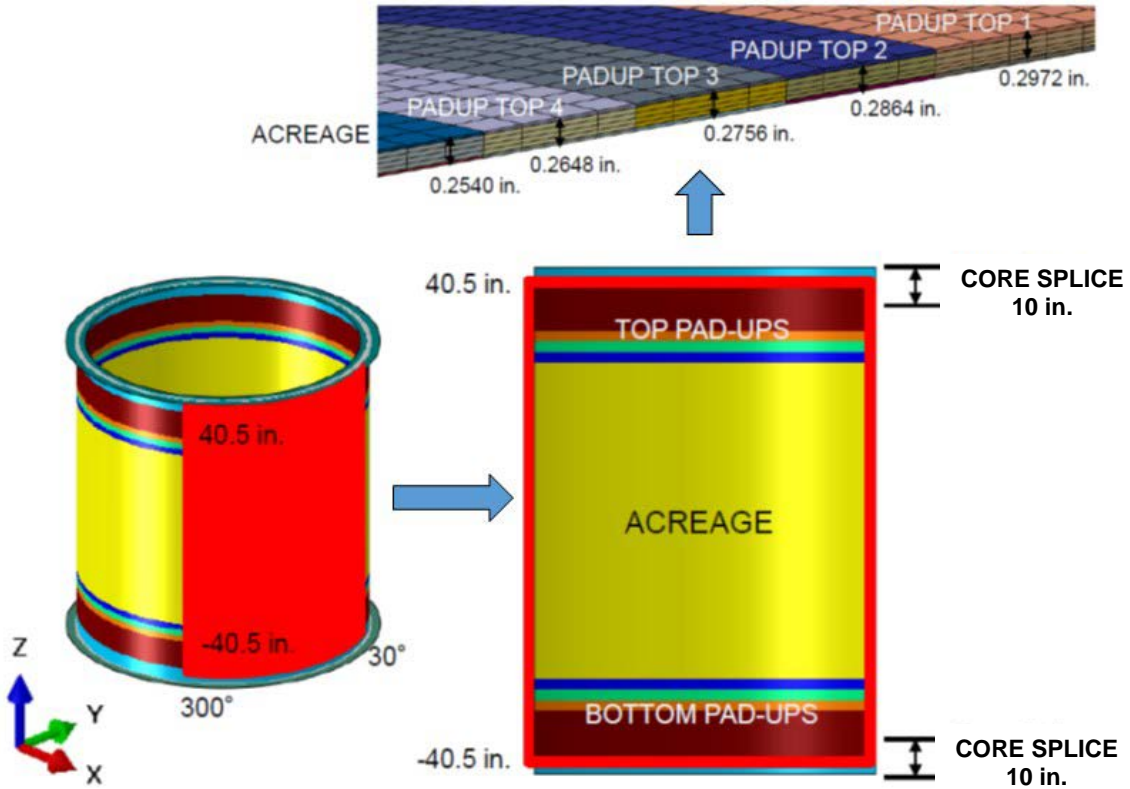
Figure 11. CTA8.3 global-local model.

The local model shown in Figure 11 comprised approximately 197,000 nodes and 232,000 elements. A geometrically nonlinear implicit solver was used to obtain solutions. In general, the approach undertaken to develop the local models permitted modeling of both radial and core thickness imperfections. However, in the results presented, only the radial imperfections were included in the CTA8.3 global-local analysis.

4.0 Finite Element Analysis and Results

In general, several FEA solvers were used in the effort. First, linear eigenvalue analyses were performed as they were anticipated to produce buckling loads close to those obtained via the closed-form solutions. Next, quasistatic linear and geometrically nonlinear static analyses were performed to aid in designing the pad-ups, and to assess the effects of nonlinear behavior in the prebuckled response. Finally, implicit transient geometrically nonlinear analyses with quasistatic loading were executed to predict the displacement and strains in the prebuckling and

into the postbuckled response regime (a nonlinear implicit transient analysis was often preceded, at the low load levels well below the buckling load, by a quasistatic nonlinear analysis to reduce the simulation runtime). For brevity, only the eigenvalue analysis and transient nonlinear results are discussed in this section. However, before the general results are presented, considerations pertaining to the stability of the numerical solution of the perfect models are discussed.

4.1 Numerical Stability of Perfect Models

One additional variation of the perfect shell FEM (i.e., in addition to that discussed in Section 3.2) was used in the nonlinear transient analyses for designs CTA8.2B and CTA8.3. The solutions for these two designs were found to be exceptionally numerically stable in their perfect configurations (the default numerical damping was used in the Abaqus nonlinear transient analyses for all four cylinder designs), which manifested itself in developing an extensive load plateau in the proximity of the buckling load. At the onset of the load plateau, the axial shortening of the cylinder would continue to increase while the corresponding load level would remain almost unchanged, as shown in Figure 12 for CTA8.3. At the same time, the radial deformations, which were axisymmetric deformations, would grow in magnitude while maintaining a stable and the very regular shape. The comparison of the predicted radial deformation (excluding the potted region) at the onset of the load plateau and at the end of the plateau for CTA8.3 is presented in Figure 13. The results plotted in the figure show that in the load-plateau region, the number of axial half waves remains the same as the radial deformation amplitude grows from 0.12 in. to 0.24 in., or by 100%, while the load level remains virtually unchanged. The Abaqus implicit transient solver does not accept negative roots in the stiffness matrix, so the equilibrium is predicted to be stable in this plateau region. This plateau is likely an unrealistic response that would not be seen in experiments for the class of shells considered in this study because small geometric, loading, or material imperfections can lead to a nonaxisymmetric response that does not show the plateau behavior. Element type, discretization, numerical imperfections, artificial solution damping, and the convergence criteria of the FEA solver, however, are all likely to influence the predicted length of the load plateau past the knee in the load versus end shortening curve. Therefore, one should not interpret too much from the predicted length of the load plateau. One method to deal with this plateau during design is to use the knee in the load versus end shortening curve as the buckling load in a way similar to how buckling is often classified for structures with a stable postbuckling response like beams, plates, or shallow-shells. However, the method of addressing the plateau behavior in this study was to randomly perturb the mesh by adjusting the nodal locations axially and circumferentially, while maintaining the perfect geometry (i.e., maintaining nominal radial locations). A random perturbation of up to 20% of the element edge length was allowed for each node in the acreage area, i.e., excluding the load-introduction rings and pad-ups. Given the chosen mesh parameters, an axial perturbation of up to ±0.1 in. and a circumferential perturbation of up to ±0.1° (or approximately ±0.08 in.) were allowed. The mesh perturbation approach for the perfect model was effective in triggering buckling without the extensive load plateau, as shown in Figure 12. When the displacement and strain results at incipient buckling obtained from the model with the perturbed mesh were compared with those obtained using the unperturbed model at the same load level, they were virtually identical. Therefore, no indications were found that perturbing a perfect-configuration mesh would result in altering the solution at loads less than the level where the load-

displacement plateau develops. Finally, the load plateau was not observed in any of the analyses performed on the geometrically imperfect models.
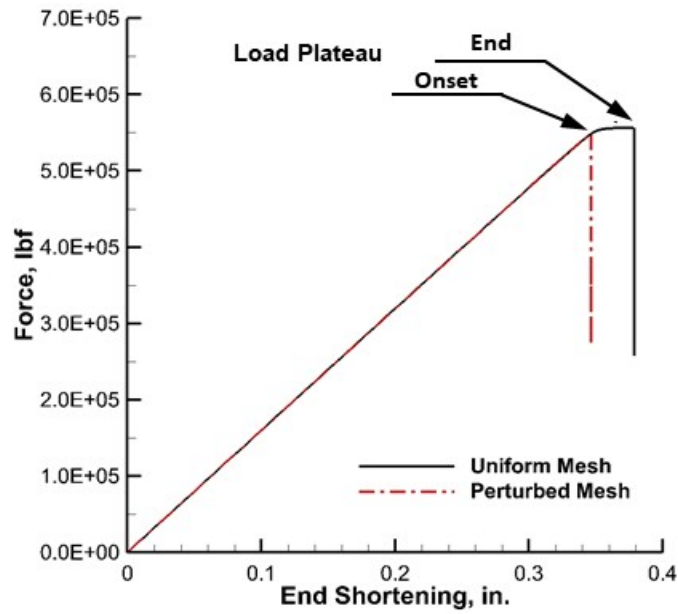

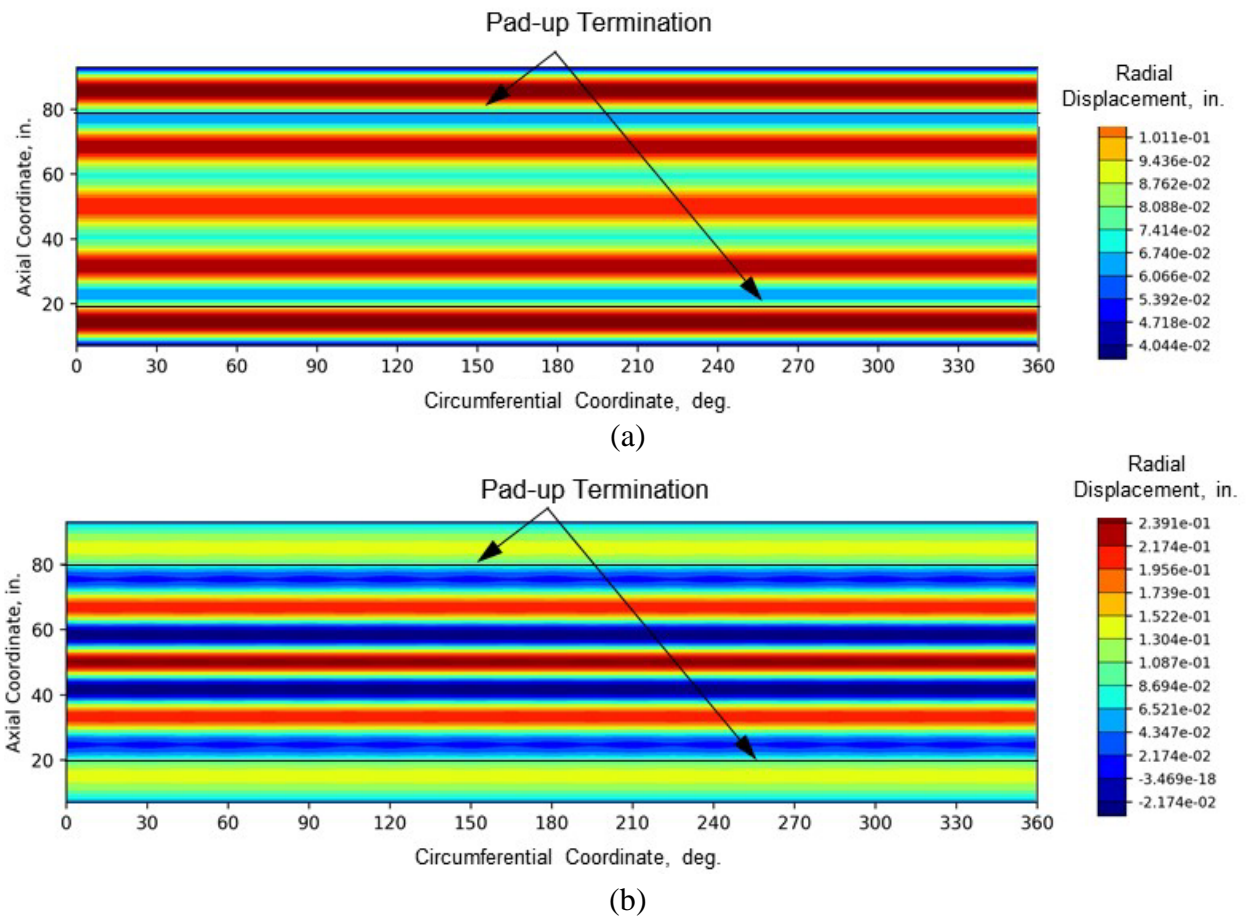Figure 12. Load plateauing behavior as observed in CTA8.3 analysis.

(a)

(b)

Figure 13. CTA8.3 radial displacement unrolled contour plot: (a) at the onset and (b) end of the load plateau.

23

4.2   Comparison with the Closed-Form Solutions

This section contains a comparison of the closed-form results with the results obtained from eigenvalue and transient nonlinear FEA. Of note is that the closed-form analyses considered idealized boundary conditions and only the acreage design, while the shell FEA, as described in Section 3.0, included the attachment rings and pad-ups representing a departure from the idealized end conditions.

The closed-form buckling loads and the finite element eigenvalue analysis buckling loads for the perfect cylinder configurations are shown in Table 7. Buckling load agreement with the test buckling load was achieved with the largest difference between the closed-form solution and the finite element eigenvalue analysis of only 4.3% for CTA8.5, and the average difference for all four designs of 2.7%. The fact that the closed-form solutions were consistently lower than the finite element eigenvalue analysis buckling loads was not surprising because the latter models included the load introduction rings and pad-up, both of which added stiffness to the ends that was not accounted for in the closed-form analysis. The buckling loads obtained from the nonlinear transient FEA with the perfect geometry were also quite close to those obtained from the FEA eigenvalue analysis, with the largest difference of only 3.4% being observed for CTA8.2B. No consistent trend was observed between the linear and nonlinear FEA buckling loads—the nonlinear analyses yielded lower buckling loads than the respective eigenanalyses for CTA8.2B and CTA8.3; the two values were nearly identical for CTA8.4; and the nonlinear buckling load was slightly higher than that obtained from the eigenanalysis for CTA8.5. When the buckling loads from nonlinear transient shell analysis with geometric imperfections were compared to any results based on the perfect configuration (closed-form, eigenanalysis, nonlinear transient), they consistently yielded lower buckling loads with the single exception of CTA8.5 where the closed-form buckling predictions was lower than the geometrically imperfect nonlinear transient buckling prediction.

Table 7. Comparison of buckling loads.

| Design | Perfect cylinder, lbf | | | Imperfect cylinder, lbf |
	Closed-form	Eigenvalue FEA	Nonlinear transient FEA	Nonlinear transient FEA
CTA8.2B	0.973×10^6	0.980×10^6	0.948×10^6	0.863×10^6
CTA8.3	0.541×10^6	0.555×10^6	0.539×10^6	0.530×10^6 [*]
CTA8.4	1.27×10^6	1.31×10^6	1.31×10^6	1.24×10^6
CTA8.5	1.15×10^6	1.20×10^6	1.21×10^6	1.16×10^6

[*]Only midsurface imperfection considered (no thickness imperfection); see discussion in Section 4.3.2.

More significant differences between the solutions for the perfect configurations were noted when considering the facesheet axial strains presented in Table 8. The predicted axial strains from the nonlinear shell FEA were always larger (more negative) than the corresponding strains from the closed-form solutions. This relationship can be attributed to the fact that the closed-form solution considered only the membrane strain and the bending strain component was a large contributor to the total strain in the nonlinear shell FEA-based analyses. When perfect configurations were considered, the nonlinear shell FEA-based strain predictions were larger by 10.9% (CTA8.2B) to 13.3% (CTA8.3). The difference between the predicted strains shown in Table 8 was greater when comparing the closed-form predictions to the perfect FEA than the difference between the predicted strains from the perfect and imperfect FEAs. In other words, the ability to capture the bending strain contribution with nonlinear analysis appeared to be more significant than the ability

to include the as-manufactured geometric imperfections. While including the geometric imperfections might have been expected to promote the strain growth rate with the increased loading, thus leading to higher bending strains, this increased strain growth rate was offset by the lower buckling loads predicted with the geometric imperfections. That is, a lower buckling load of the imperfect FEA became a compensating factor suppressing the strain growth beyond that of the perfect configuration. One other interesting observation pertained to CTA8.3, which was the only design considered without the core thickness imperfections. In Table 7, the buckling load difference between the perfect and imperfect FEA solutions was the smallest (−1.7%) of the four configurations (the differences for the remaining three designs were between −4.3% and −9.8%). In Table 8, CTA8.3 was the only configuration where the imperfect FEA yielded higher strains then the perfect one. The application of the radial imperfections only possibly reduced the buckling load by a relatively small amount that was not sufficient to compensate for the higher strain rate growth as observed in other configurations analyzed with both radial and thickness imperfections.

Table 8. Comparison of axial strains corresponding to buckling loads.

Design	Perfect cylinder, $\mu\varepsilon$		Imperfect cylinder, $\mu\varepsilon$
	Closed-form	Nonlinear transient FEA	Nonlinear transient FEA
CTA8.2B	-4959	-5566	-5319
CTA8.3	-3902	-4503	-4782[*]
CTA8.4	-4454	-5085	-5021
CTA8.5	-3917	-4484	-4470

[*]Only midsurface imperfections considered (no thickness imperfection); see discussion in Section 4.3.2.

4.3 Detailed Results

In this section, the results obtained from the nonlinear transient analyses for CTA8.3 are presented and discussed. The solutions obtained for the perfect cylinder configurations are introduced and discussed in Section 4.3.1 and include the shell-element- and axisymmetric-element-based analyses. The solutions obtained for the imperfect cylinder configurations are introduced and discussed in Section 4.3.2 and include the shell-element-based and global-local analyses. The results discussed in this section include axial and radial displacements, facesheet axial and hoop strains, core and core-to-facesheet normal and shear stresses, and failure indices.

The shell-element-based nonlinear analysis results were examined by reviewing the radial and axial cylinder deformations, the axial and hoop strain distributions, and the Tsai-Hill failure indices (using the built-in Abaqus functionality),[17] especially in the proximity of the buckling load. The axial compressive strain and Tsai-Hill criterion results received particular scrutiny to ensure that the structures would experience global buckling response prior to the strength failure. The response curves showing applied load versus cylinder end shortening (i.e., relative displacement of the attachment rings) and versus actuator displacement (i.e., the displacement of the load lines at the actuator) were examined. While the former were a design performance metric, the latter were of interest for test monitoring.

The total load applied to the CTA8.3 cylinder versus the end shortening, obtained from the simplified FEM as defined in Figure 7, is presented in Figure 14. The perfect cylinder was predicted to buckle at 0.539×10^6 lbf and the imperfect cylinder (radial imperfections only) was predicted to buckle at 0.530×10^6 lbf, which is 1.7% lower load than the perfect configuration. Both perfect and imperfect cylinders exhibited a nearly linear load versus displacement response

to the buckling load. By comparing the buckling load obtained from the simplified FEMs with the attachment rings only (Table 7) and the buckling load obtained from the FEMs with the entire load-introduction setup, Figure 14, it was observed that the two loads agree within three significant digits for both perfect and imperfect configurations. The fact that the same buckling loads were obtained from the models with and without the test stand can be explained by examining the axial displacement results at incipient buckling, shown in Figure 15. The axial displacement gradient within the test article was large when compared with the axial displacement gradients within the load introduction fixtures above and below the test article. This observation indicated that the stiffness of the load introduction fixture was much larger than that of the test article itself. Therefore, the idealized load introduction in the simplified FEM applied by uniform axial displacement of the metallic load introduction rings was nearly identical to that of the test setup. Consequently, all the subsequent results obtained from the shell analysis were obtained from its simplified model variant with the metallic load introduction fittings only. In the remainder of this section, the strains, displacements, and failure indices obtained from the shell-element-based analysis are shown as unrolled contour plots to provide a spatially complete depiction of the cylinder response. Axial and hoop strain results are presented on the surface of the cylinder (OML or IML) that has the minimum (most compressive) axial strain values. The Tsai-Hill criterion results are presented using the composite plot combining peak values at a given shell location irrespective of the ply at which they occurred, and the single ply plot, for the ply where the critical value was identified. Black horizontal lines near the top and bottom of each unrolled plot depict the limits of the pad-up plies, as shown in Figure 16.
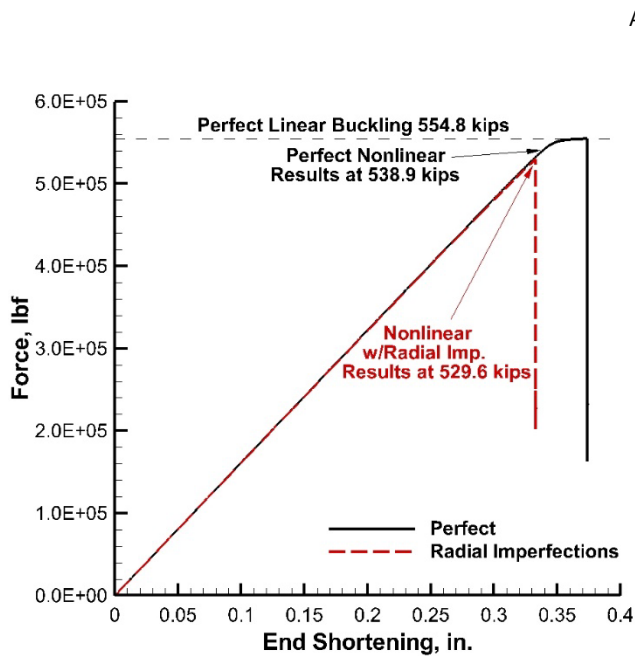

Figure 14. Load versus displacement of the perfect and imperfect CTA8.3 cylinders using the simplified FEM.
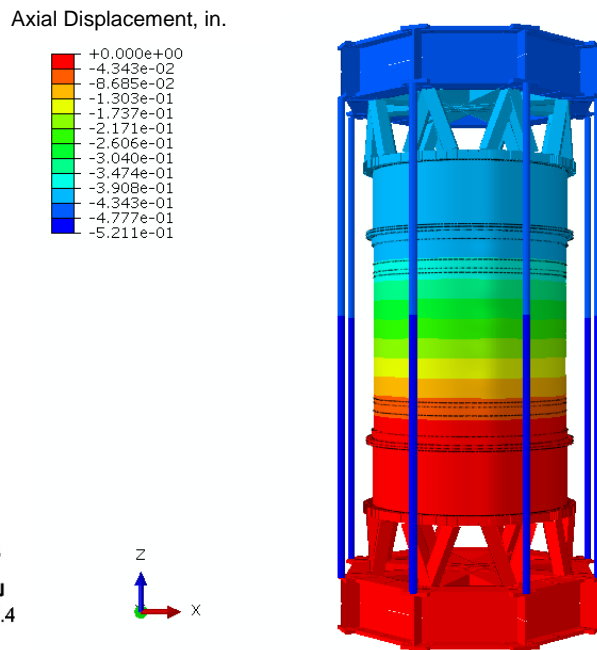
Figure 15. Imperfect CTA8.3 axial displacement at incipient buckling.
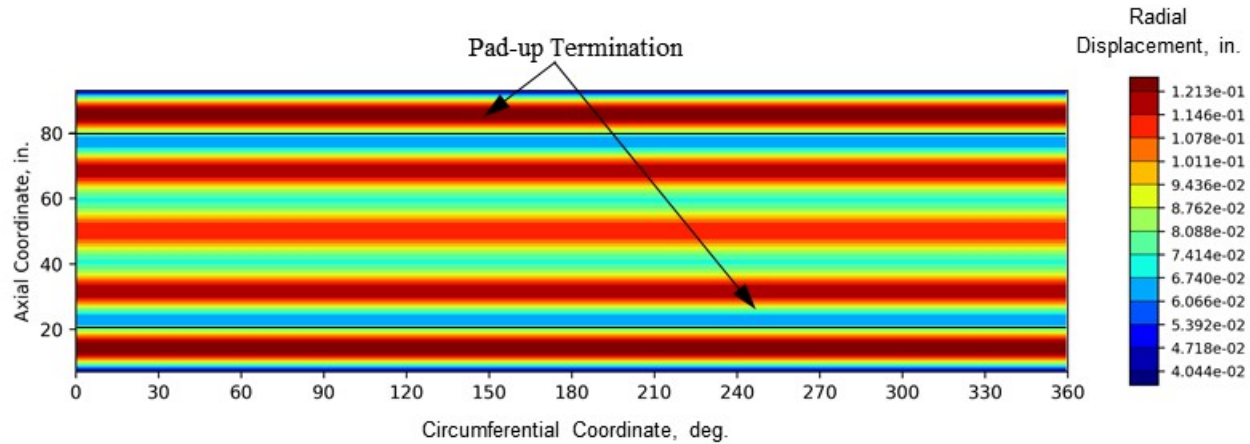
26

Figure 16. Perfect CTA8.3 radial displacement at incipient buckling.

The axisymmetric-element-based analysis results for the perfect model and the global-local analysis results from the imperfect model were reviewed with primary focus on the core performance metrics and core-to-facesheet interactions; core crush and transverse shear stresses received particularly close attention. The axisymmetric model was first checked against the results obtained from the shell FEA. This comparison involves examining the end shortening versus the applied load and the radial deformations. Next, particular attention was dedicated toward evaluation of the modeling assumptions applied at the potted ends of the cylinder. Specifically tied and sliding interactions within the potted sections of the cylinder were explored.

When reviewing the global-local model results, again the preliminary checks were accomplished by comparison with the shell-element-based analysis. This comparison included scrutinizing the extent of the local model interference with global model boundaries. Finally, the core performance and core-to-facesheet interaction metrics were captured. Similar to the axisymmetric-element-based model, core crush and transverse shear stresses were of primary interest.

Apart from specific strain or stress response metrics, failure indices were computed to perform assessments across different failure modes and identify the most critical one.

4.3.1 Perfect Model

Contour plots of the predicted radial displacements, the axial strain and the hoop strains of the perfect CTA8.3 at incipient buckling are presented in Figures 16, 17, and 18, respectively, and the Tsai-Hill failure criterion is presented in Figure 19. At the incipient buckling load, the cylinder exhibited five rings of the outward radial displacements, three of which were within the acreage area, and one of which was in each of the top and bottom pad-up areas, as shown in Figure 16. The maximum radial displacement of 0.12 in. was identified in the pad-up area so it comes as no surprise that the maximum hoop strain of 2652 $\mu\varepsilon$ (Figure 18) was also identified in this area. The maximum compressive strain was 4503 $\mu\varepsilon$ (Figure 17) and was located in the acreage area, i.e., the section with fewer facesheet plies when compared to the pad-up area. The relationship between the axial and hoop strains was typical for all the considered test article designs (not shown), i.e., that the absolute value of the maximum compressive axial strain was significantly larger than the

maximum tensile hoop strain and that the axial strains were likely more critical. This observation was substantiated by the failure index results, defined in Eq. 12 and shown in Table 9.

$$\text{Failure Index} = \frac{\text{Analysis Result}}{\text{Allowable}} \tag{12}$$

Specifically, the failure indices based on the axial strains only and using the Tsai-Hill failure criteria produced very similar values, indicating that the hoop strain component was not a dominant factor in the response. It was also not surprising that the maximum compressive strain occurred on the IML surface of the acreage section that was experiencing a large outward deformation. At such location, the membrane compressive strain and the peak compressive strain from the bending in the axial direction were additive. This observation was confirmed using the Tsai-Hill failure criterion results (see Figure 19). First, the envelope plot compiling the maximum index at a given location and irrespective of the ply, shown in Figure 19(a), was examined. Next, using the maximum index value, all plies were examined individually to identify the one that produced the largest Tsai-Hill index. Indeed, the innermost ply of the IML facesheet, shown in Figure 19(b), was the one that produced the largest index.
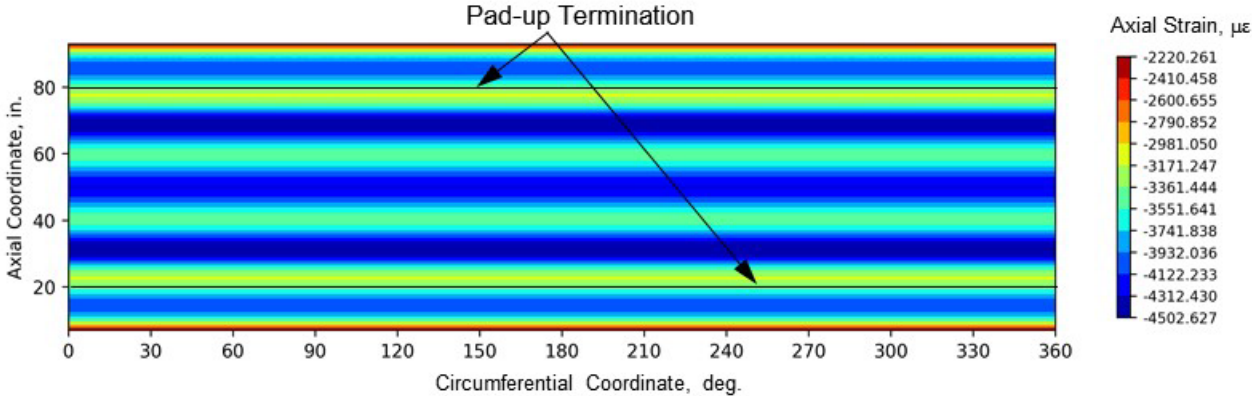

Figure 17. Perfect CTA8.3 IML axial strain at incipient buckling.
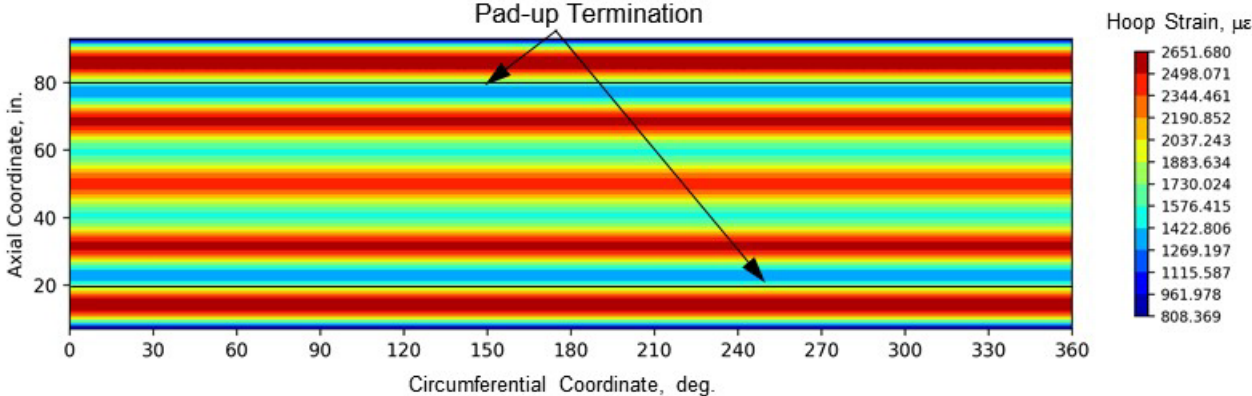
Figure 18. Perfect CTA8.3 OML hoop strain at incipient buckling.

(a)

(b)
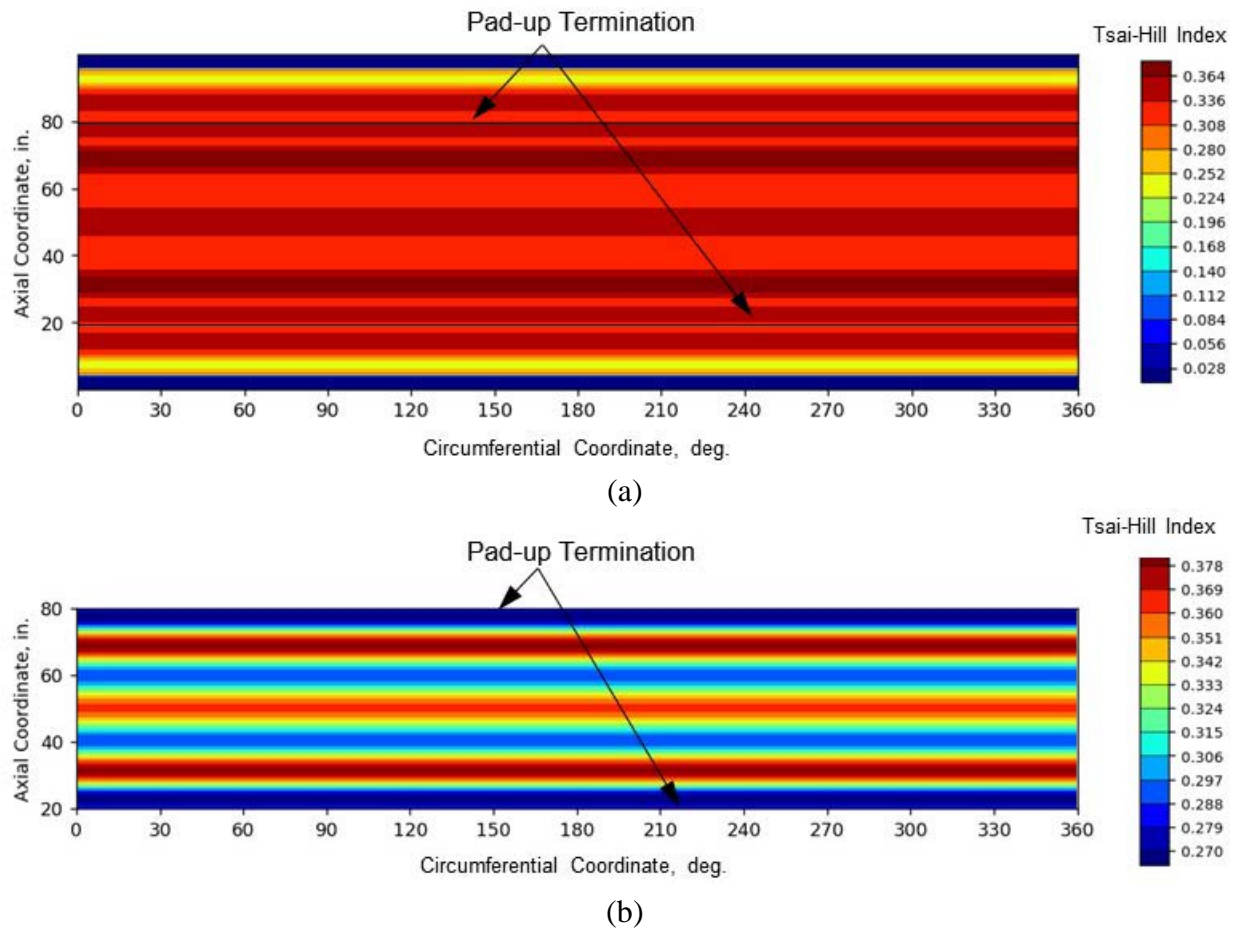
Figure 19. Perfect CTA8.3 Tsai-Hill failure criterion at incipient buckling: (a) envelope for all plies and (b) innermost IML facesheet ply.

The strain-based failure indices, shown in Table 9 (and subsequent tables with failure indices from the shell-element analyses), were calculated using test results from Reference 12 as Allowable in Eq. (12). The Tsai-Hill-based failure index, shown in Table 9 (and subsequent tables with failure indices from the shell-element analyses), was calculated using the co-cure sandwich knockdown factor (KD), introduced and derived in Appendix E, as Allowable in Eq. (12). The co-cure sandwich knockdown factor was a means of accounting for sandwich facesheet property degradation relative to the solid laminate and the solid laminate properties from Reference 13 were used to produce the Tsai-Hill indices.

Table 9. Summary of the shell-element-based results for perfect CTA8.3 model.

Measure, Unit	Axial Strain, $\mu\varepsilon$	Hoop Strain, $\mu\varepsilon$	Tsai-Hill Index
Value	-4503	2652	0.379
Failure Index	0.57[*]	0.15[**]	0.53[***]

[*] Computed using -7926 $\mu\varepsilon$ compression allowable (Ref. (12))

[**] Computed using 17,400 $\mu\varepsilon$ tension allowable (Ref. (12))

[***] Computed using 0.71 co-cure sandwich knockdown factor (Appendix E)

The axisymmetric-analysis results were first checked against the already available shell-element-based analysis results. Specifically, the load-end shortening curves and radial displacement profiles in the proximity of the predicted failure load were selected for the comparison and are

shown in Figure 20. The load-end shortening agreement shown in Figure 20(a) was favorable overall, with the axisymmetric-element-based analysis with the sliding boundary condition showing slightly softer response than the remaining analyses. The axisymmetric-element-based analysis with the sliding boundary condition was the only analysis in Figure 20(a) where relative movement between both test article facesheets and the potting grout within the load introduction fitting was permitted and observed to take place, including observed separation of the IML facesheet from the grout. This modeling feature and response characteristic was likely responsible for the increased compliance of the sliding boundary model relative to the remaining models. The agreement of the radial displacement profiles, shown in Figure 20(b), was also good overall, especially when the far field results away from the load introduction fitting/potting area were considered. The axisymmetric-element-based analysis solution using the sliding boundary condition appears to be in the best agreement with the shell-element-based analysis solution, while the axisymmetric-element-based analysis solution with the sliding IML/tied OML boundaries appeared to compare least favorably. To better interpret the results in Figure 20(b), it was important to consider that the radial displacement in the shell-element-based model was obtained from a single node located approximately in the midsurface of the element. Furthermore, in the load introduction fitting area, the shell element model had a significant thickness that accounted for the metallic load introduction fitting, potting grout, and the sandwich cylinder wall with the pad-up plies. The radial displacements for all the axisymmetric-element-based model variants were obtained from the most outer node of the OML facesheet. While radial displacements obtained from the two distinct model types and node locations were perceived as comparable outside the load introduction fitting, the comparison within the fitting was likely more affected by the modeling differences discussed in this section. Therefore, the best agreement between the shell-element-based analysis results and the axisymmetric-element-based analysis results with the sliding boundary might have been incidental due to the modeling oversimplification on the part of the shell-element-based model in the load introduction fitting section.
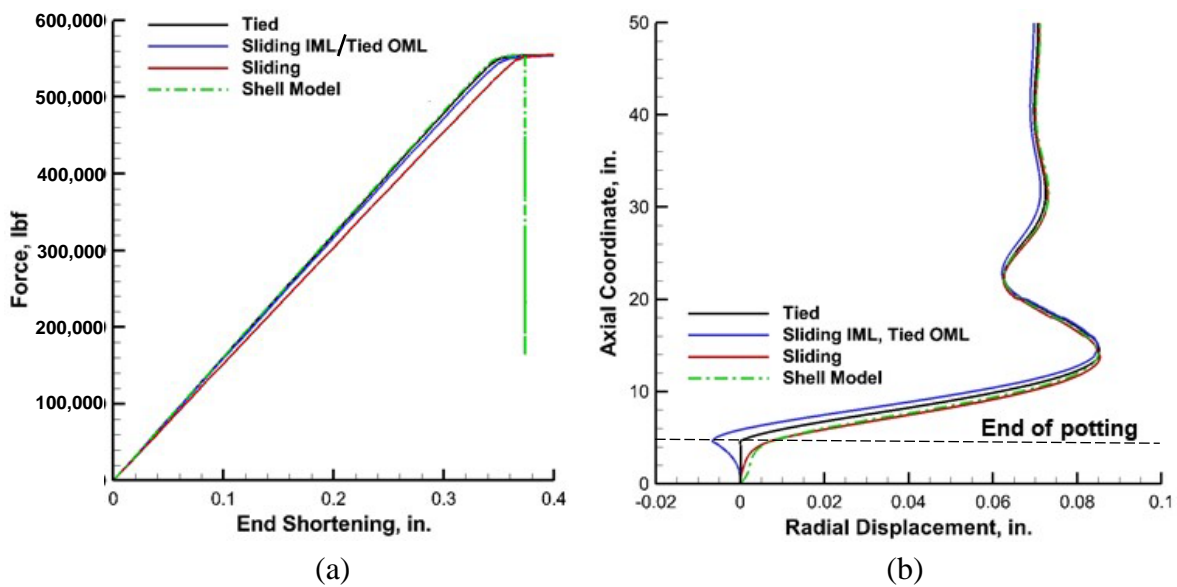

Figure 20. (a) Load versus end shortening and (b) radial displacement profiles of perfect CTA8.3 at 400 kip.

The general areas of high crush and transverse shear stresses identified by the axisymmetric analyses are highlighted in Figure 21. The peak crush stresses were identified on the OML side of the honeycomb core at the location coinciding with the termination of the load-introduction rings, as shown in Figure 21(a). This result was quite intuitive due to the abrupt change in the radial stiffness occurring at this location. High transverse core shear stresses were identified at two locations, one above and one below the termination of the load introduction ring webs, as shown in Figure 21(b). As in Figure 21(b), the location above the web termination extended farther away from the edges of the ring web (the section of the core shown in red) than the location within the ring grove (the section of the core shown in blue). Finally, the spatial extent of the high transverse shear stresses and the peak stress location varied only slightly (not shown) according to the type of interactions (tied, sliding, or sliding IML/tied OML) assumed between the sandwich cylinder wall and the potting grout, as described in Section 3.2.2.
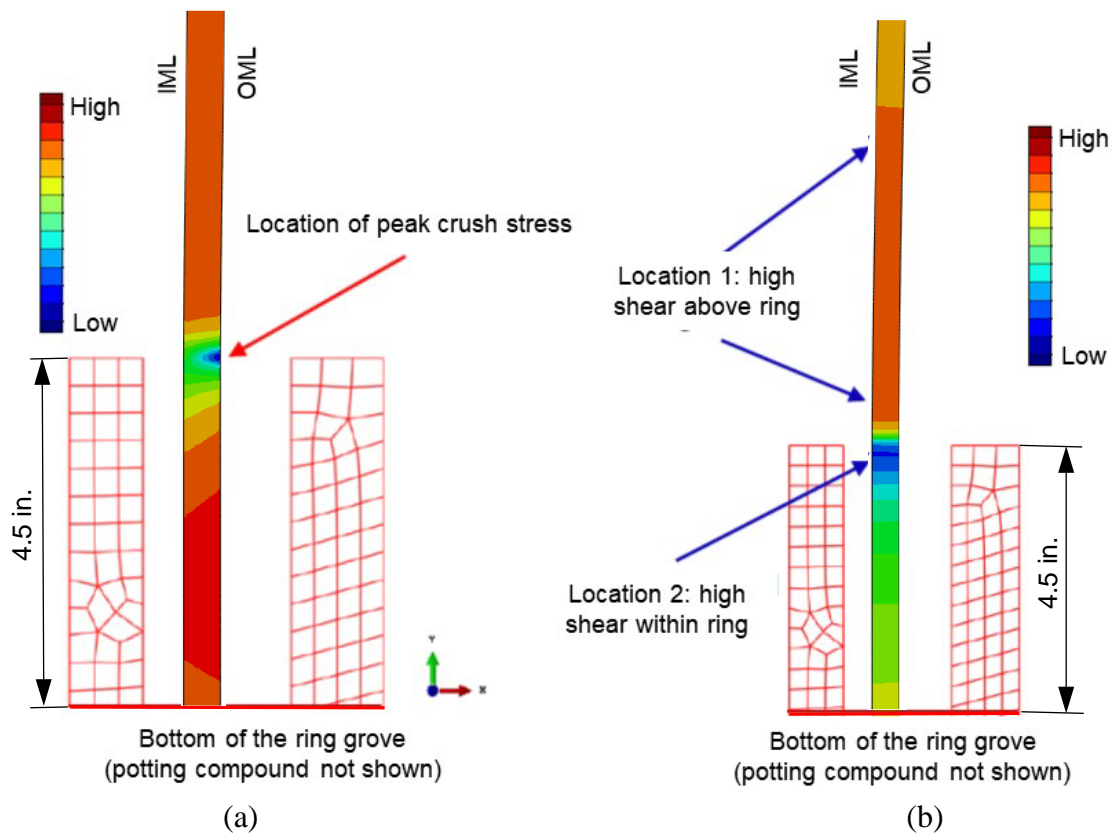
Figure 21. Characteristic locations of (a) high crush and (b) transverse shear stresses obtained from the CTA8.3 axisymmetric-element-based model.

The peak crush and transverse shear stresses inside and outside the load introduction ring are shown in Table 10. For each metric in Table 10, two failure indices were computed—one based on the typical and one based on the minimum core allowable stresses as published by the manufacturer.[14] The core crushing was the more critical failure mode when compared to the core transverse shear, as shown in Table 10. The absolute values of the core transverse shear were higher at the location within the ring (Location 2) than outside the ring (Location 1). The boundary interactions other than sliding could result in the premature failure of test article, especially if an adhesive bond developed and was sustained throughout the entire test sequence. More specifically, when the minimum crush core properties were considered, the failure index of 1.42 was obtained

for the fully tied interaction, and the failure index of 1.09 was obtained for the sliding IML/tied OML interaction. Since the failure index of one or greater indicates failure, this observation further emphasized the importance of the proper application of the release agent during the potting operation. It also showed how sensitive the load introduction design was to, what could be perceived as minor, details of the test article preparation.

When reviewing the core analysis results, of note was the fact that the two failure modes were considered in isolation. In other words, the homogenized treatment of the core did not facilitate accounting for the cumulative effect of core crushing and transverse shearing.

Table 10. Crush and transverse shear stresses in the 8.1 pcf core in the vicinity of the end ring for different boundary condition modeling in the CTA8.3 axisymmetric-element-based model at 539 kips.

End Boundary Condition	Crush Stress, psi	Failure Index		Transverse Shear Stress Loc. 1, psi	Failure Index		Transverse Shear Stress Loc. 2, psi	Failure Index	
		Typical	Min.		Typical	Min.		Typical	Min.
Tied	1849	0.97	1.42	178	0.19	0.24	-572	0.61	0.77
Sliding	566	0.30	0.44	162	0.17	0.22	-167	0.18	0.23
Sliding IML/ Tied OML	1419	0.75	1.09	196	0.21	0.26	-546	0.58	0.74

While the results in Table 10 focused exclusively on the denser (8.1-pcf) core behavior within or in the close proximity of the metallic load introduction ring, Figures 22 and 23 show, respectively, the results pertaining to the core-to-facesheet normal stress and the shear stress over the entire test article height (only half of the total height is shown on the vertical axis due to the model symmetry). The normal stresses, shown in Figure 22, were generally low, except for a few characteristic locations. Apart from the metallic ring termination (at the 4.625-in. station), the remaining normal stress spikes were associated with the core transition from the 8.1-pcf to 3.1-pcf density (at the 10-in. station) and the pad-up ply drops (indicated with the red dashed lines at stations 14 in., 16 in., 18 in., and 20 in.). As highlighted by the axisymmetric analysis results insets on the right hand side of Figure 22, these stress spikes occurred in spatial domains confined within few individual CAX4 elements in the axisymmetric model, and were much smaller than the actual honeycomb cell sizes also depicted in the insets. This dimensional relationship, combined with the homogenized core modeling assumption, made the localized high normal stress values unreliable and essentially highlighted a limitation of the axisymmetric-element-based analysis.

The core-to-facesheet shear stresses are shown in Figure 23. Observations similar to those made for the normal stress results in Figure 22 could be made for the shear stresses as well. The shear stresses were generally low, except for a few characteristic locations. Apart from the proximity of the ring termination (the 4.625-in. station), the remaining transverse shear stress spikes were associated with the core transition from the 8.1-pcf to 3.1-pcf density (at the 10-in. station) and the pad-up ply drops (indicated with the red dashed lines at stations 14 in., 16 in., 18 in., and 20 in.). As highlighted by the axisymmetric analysis results insets on the right hand side of Figure 23, these stress spikes also occurred in spatial domains confined within few individual CAX4 elements, and much smaller than the actual honeycomb cell sizes also depicted in the insets. This dimensional relationship combined with the homogenized core modeling assumption, made the localized high shear stress values unreliable and essentially again highlighted the limitation of the axisymmetric-element-based analysis.
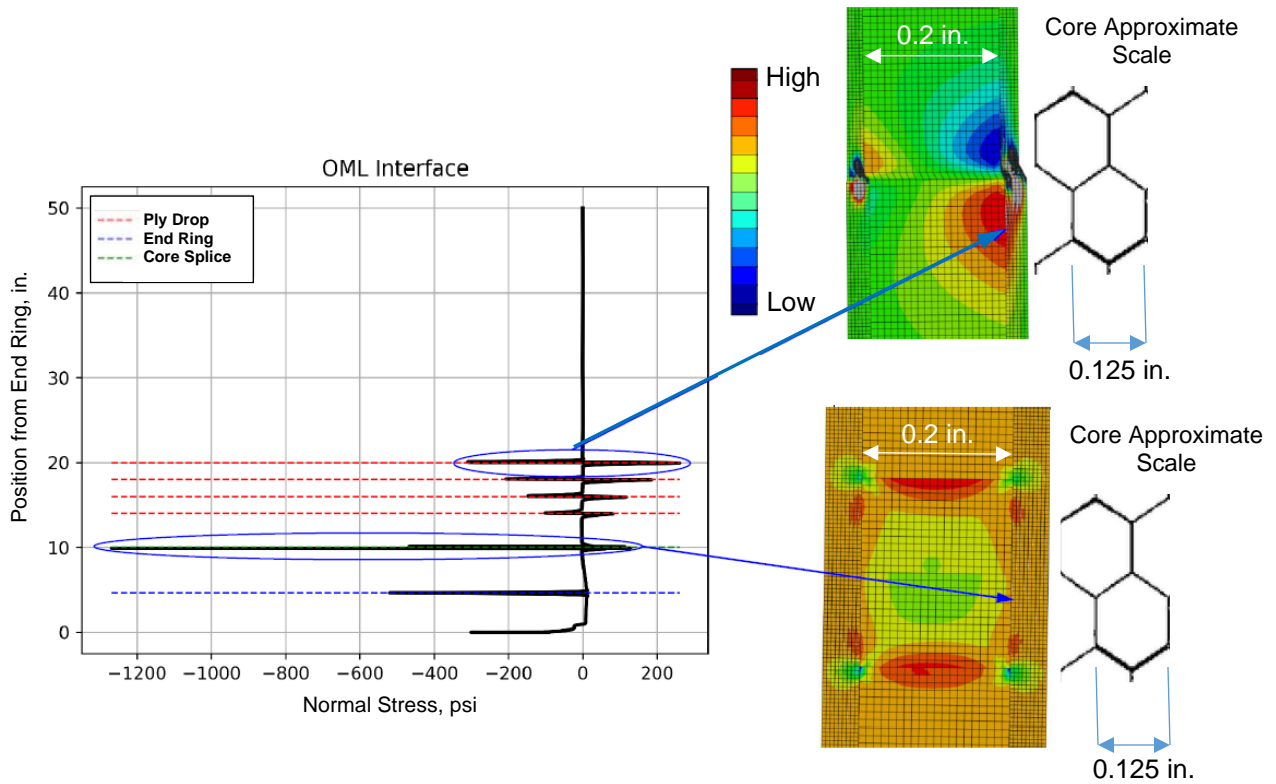
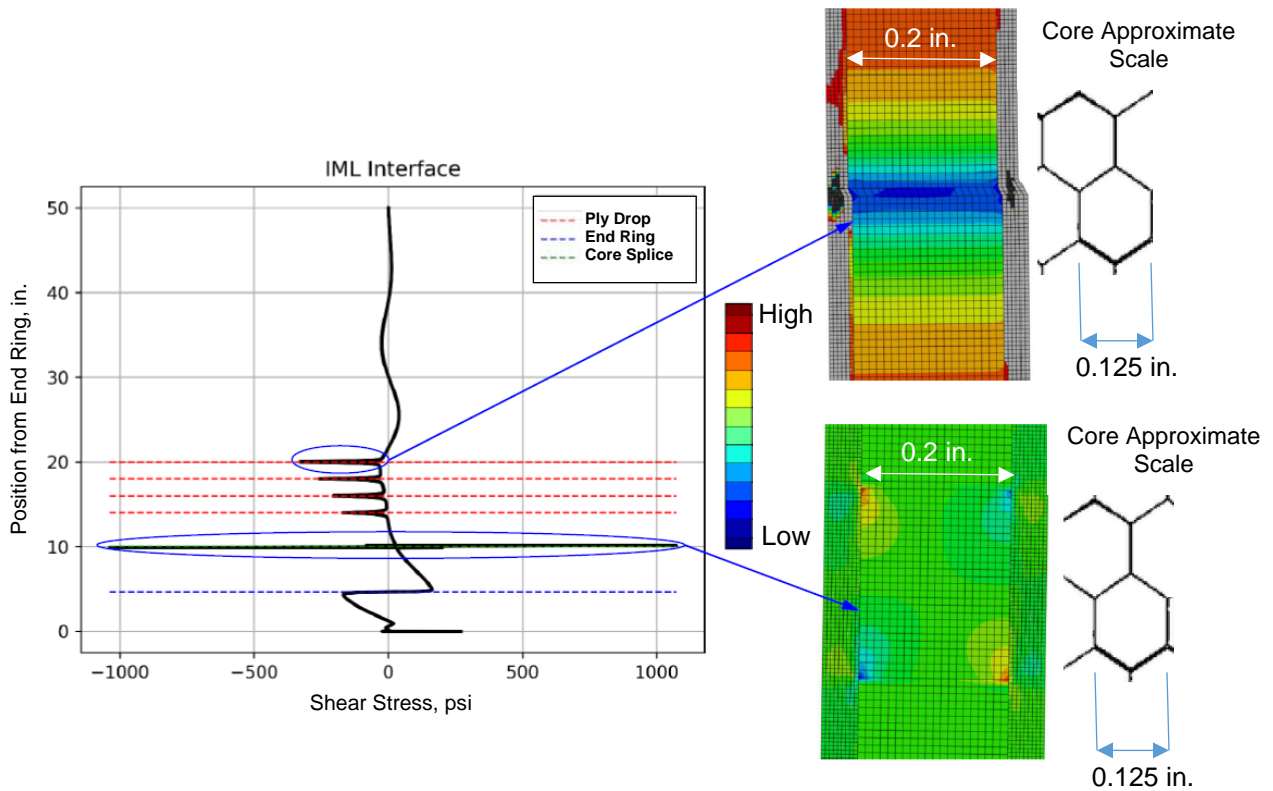Figure 22. CTA8.3 core-to-OML facesheet normal stress under 535-kip loading.

Figure 23. CTA8.3 core-to-OML facesheet shear stress under 535-kip loading.

4.3.2 Imperfect Model

The predicted radial displacements at incipient buckling of the imperfect CTA8.3 model are presented in Figure 24. The corresponding axial and hoop strains are presented in Figures 25 and 26, respectively, and the Tsai-Hill failure criterion results are presented in Figure 27. It was observed that, at incipient buckling, the cylinder exhibited a response similar to the perfect configuration shown in Figure 16 with five rings of the outward radial displacements, three of which were within the acreage area, and one of which was at each top and bottom pad-up areas. The five outward displacement rings were, however, less axisymmetric in shape, which was expected for the imperfect cylinder configuration. The maximum predicted radial displacement of 0.13 in. was slightly larger than the 0.12-in. perfect-configuration prediction and also within the pad-up area. The maximum predicted hoop strain of 2825 $\mu\varepsilon$ (see Figure 26) was also in the pad-up area and was also slightly larger than that predicted with the perfect-configuration analysis. The maximum predicted compressive strain was 4782 $\mu\varepsilon$ (see Figure 27) and was located in the acreage area. The relationship between the axial and hoop strain was similar to that of the perfect configuration in that the absolute value of the maximum compressive strain was significantly larger than the maximum tensile hoop strain. The failure indices, computed by Eq. (12), are shown in Table 11. The failure indices were only slightly larger (by 0.01 to 0.04) than those obtained from the perfect cylinder analysis (see Table 9), and reflect the similar trend that the index obtained based on the axial strain was the largest, closely followed by the one based on the Tsai-Hill failure criterion, with the one based on the hoop strain being the distant last. It was then concluded that, similar to the perfect configuration, the hoop strain component was not a dominant factor in the imperfect cylinder predicted failure response. It was also not surprising that the predicted maximum compressive strain occurred on the IML surface of the acreage section that was experiencing a large outward deformation. At such location the membrane compressive strain and the peak compressive strain from the bending in the axial direction were additive. The predicted Tsai-Hill index results were given in Figure 27. First, the envelope plot compiling the maximum index at a given shell location and irrespective of the ply, Figure 27(a), was examined. Next, using the maximum index value, all plies were examined individually to identify the one that produced the largest Tsai-Hill failure index. As was the case for the perfect configuration analysis, the innermost ply of the IML facesheet, ply 1, shown in Figure 27(b), was the one to produce the largest Tsai-Hill index, which in the imperfect case was 0.57.

Table 11. Summary of the shell-element-based results for the imperfect CTA8.3 model at 530 kips.

Measure, Unit	Axial Strain, $\mu\varepsilon$	Hoop Strain, $\mu\varepsilon$	Tsai-Hill Index
Value	-4782	2825	0.405
Failure Index	0.60[*]	0.16[**]	0.57[***]

[*] Computed using -7926 $\mu\varepsilon$ compression allowable

[**] Computed using 17,400 $\mu\varepsilon$ tension allowable

[***] Computed using 0.71 co-cure sandwich knockdown factor (reference Appendix E)
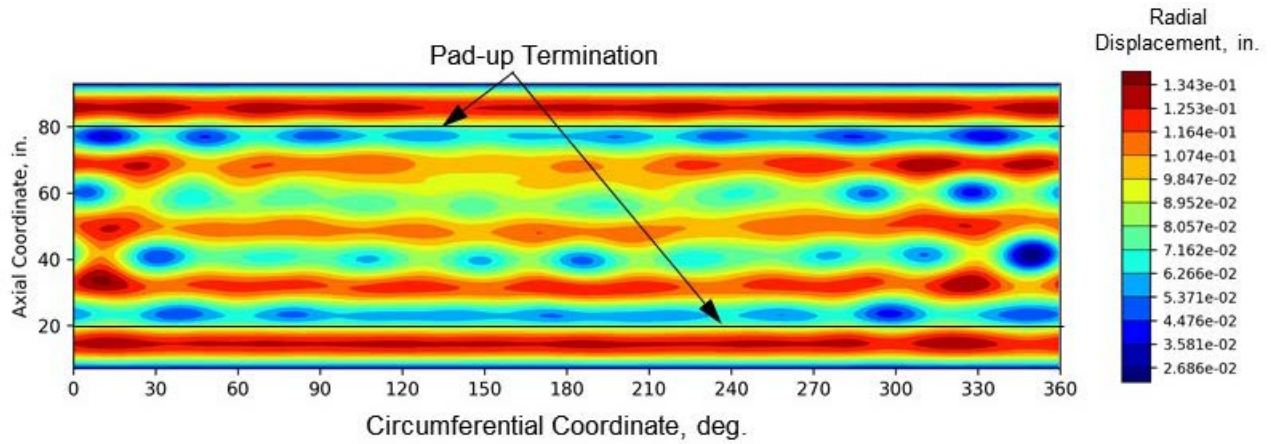
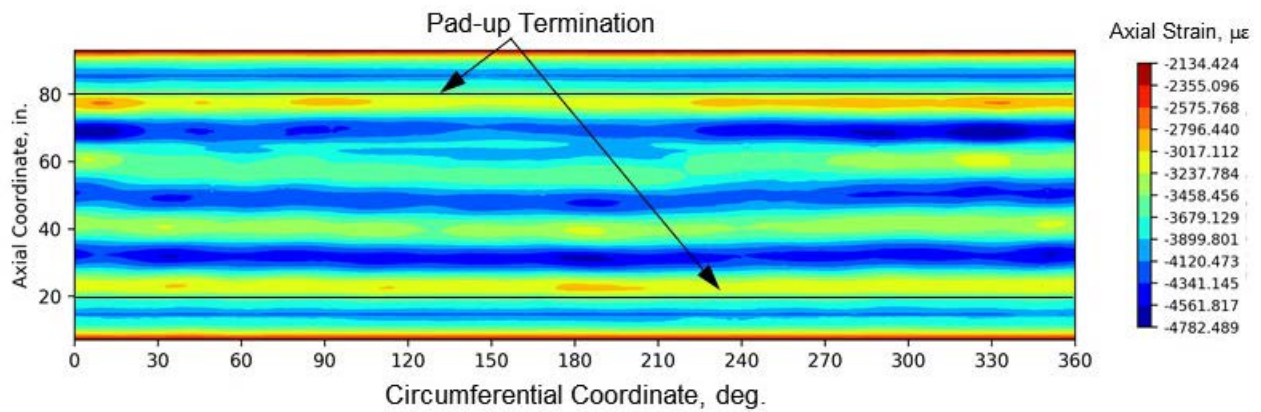Figure 24. Imperfect CTA8.3 radial displacement at incipient buckling.

Figure 25. Imperfect CTA8.3 IML axial strain at incipient buckling.
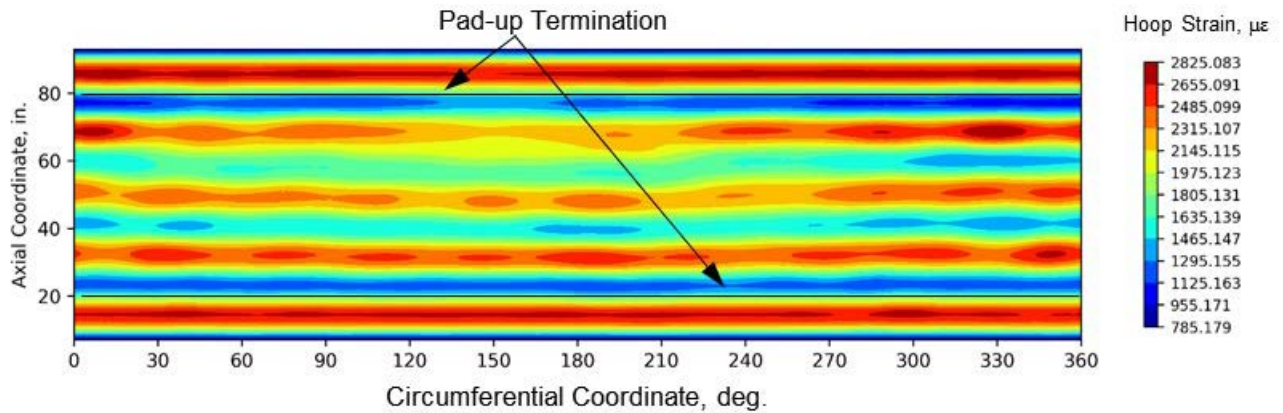

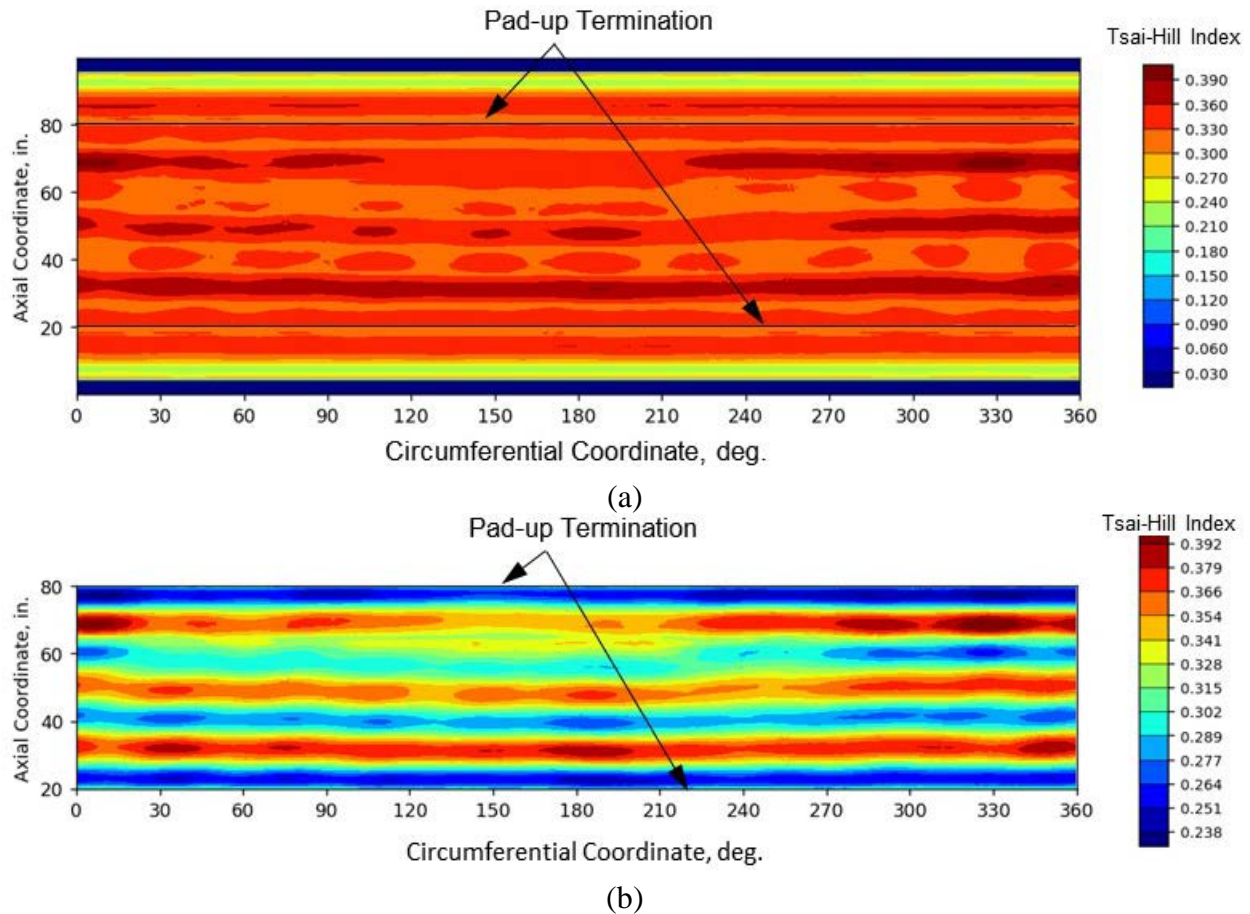Figure 26. Imperfect CTA8.3 OML hoop strain at incipient buckling.

Figure 27. Imperfect CTA8.3 Tsai-Hill failure criterion at incipient buckling: (a) envelope for all plies and (b) innermost IML facesheet ply.

Similar to the axisymmetric analysis, the process of developing the global-local analysis began with a validation effort that included: (1) comparing the total work produced within the global-local domain boundary by the nodes belonging to the local model with the nodes belonging to the global model, presented in Appendix E, and (2) checking the global-local results against those obtained from the shell-element analysis, presented next in this section.

Axial and radial displacements obtained for the local spatial domain based on the imperfect shell and local models at 480 kips, or approximately 90% of the predicted buckling load, are shown in Figure 28. While excellent axial displacement agreement was achieved, as shown in Figure 28(a), the radial displacement fields in Figure 28(b) showed small but noticeable differences. These differences could, at least in part, be explained by inherent differences in the assumptions used in the finite element architectures. Namely, the shell elements (S4R) had six degrees of freedom per node, three translational and three rotational, the behavior of the through-the-thickness deformation conformed to a certain interpolation curve order, and only one node through the entire sandwich wall thickness was used. The continuum shell (SC8R) and solid (C3D8R) elements of the local model had only three translational degrees-of-freedom per node and multiple elements were used across the thickness of the sandwich wall. Thus, the local modeling approach effectively applied fewer constraints on the deformed cross section as a larger number of degrees of freedom was available to capture the deformation, which did not have to conform to an assumed shear

deformation theory of the shell element. With the understanding of these limitations, the comparison of the radial displacement fields was determined to be acceptable.

(a)

(b)
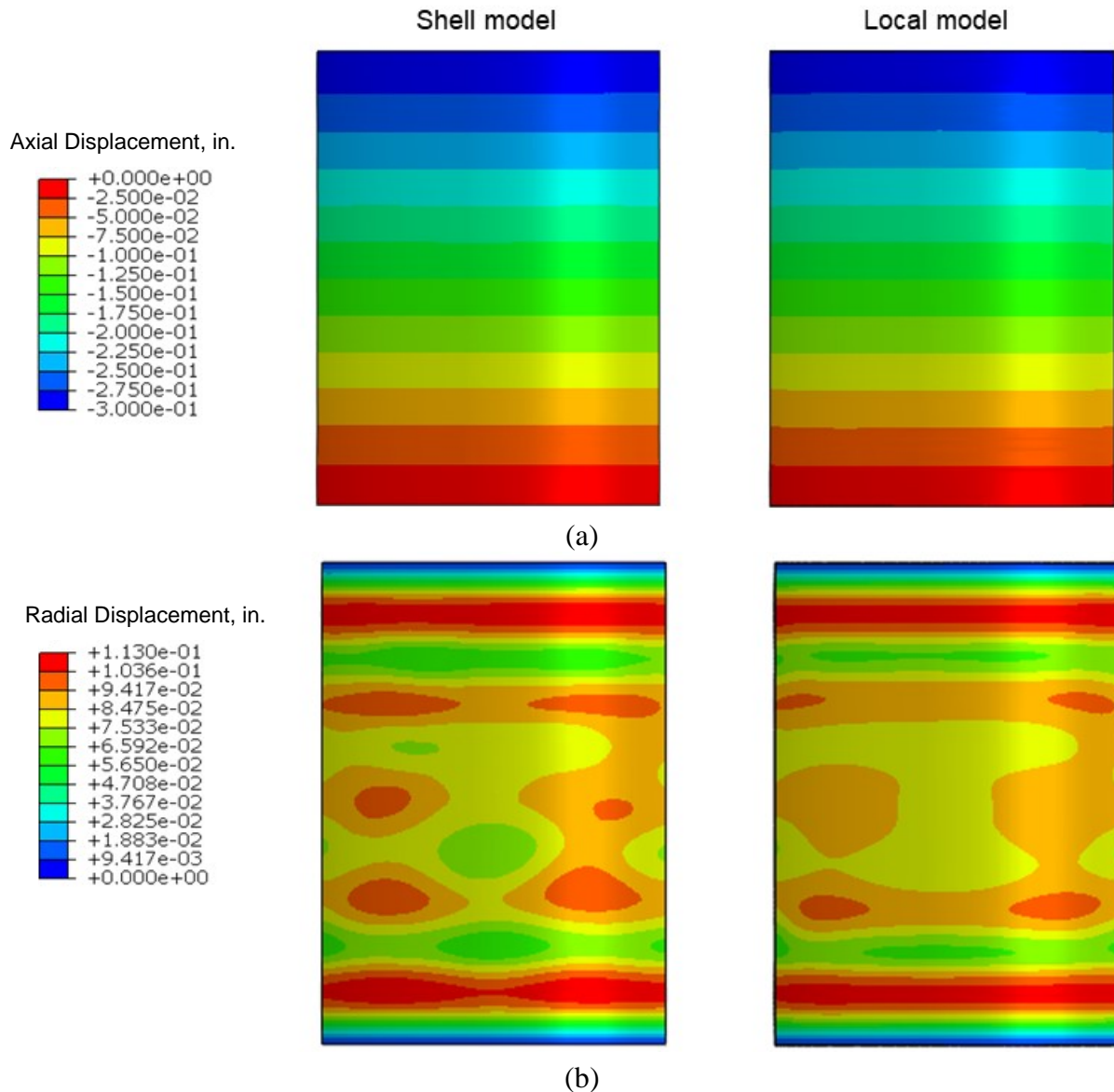
Figure 28. Comparison of the shell model and local model results for imperfect CTA8.3 at 480 kips: (a) axial displacement and (b) radial displacement.

The crush and transverse shear stress results obtained in the local domain of the imperfect global-local CTA8.3 model at incipient buckling (530 kips) are shown in Figure 29. As annotated in Figure 29, the spatial domain of the local model included the transition from the denser 8.1-pcf core to the lighter 3.1-pcf core and termination of all the pad-up plies but did not include the termination of the metallic load introduction ring. The minima and maxima core stresses are summarized in Table 12, which also includes the summary of the facesheet axial and hoop strains, as well as the Tsai-Hill failure criterion indices. All results had their respective failure indices computed per Eq. (12), with the honeycomb-core indices computed based on both typical and minimum values.
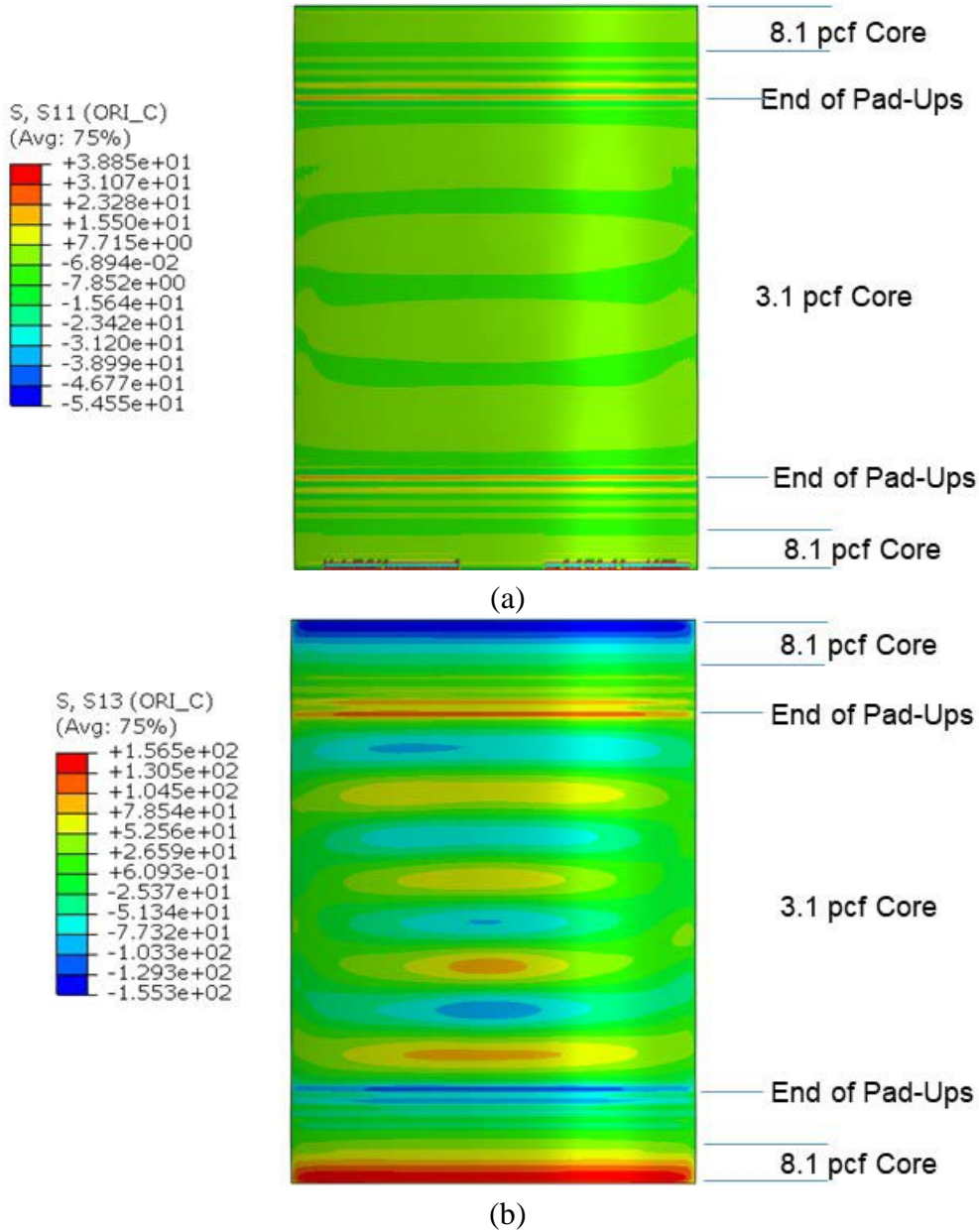
Figure 29. Core results from the imperfect CTA8.3 global-local analysis at incipient buckling: (a) crush stress and (b) transverse shear stress.

Table 12. Summary of the global-local results for imperfect CTA8.3 model at incipient buckling.

	Facesheets			3.1 pcf Core		8.1 pcf Core	
Measure, Unit	Axial Strain, με	Hoop Strain, με	Tsai-Hill Index	Crush Stress, psi	Transverse Shear Stress, psi	Crush Stress, psi	Transverse Shear Stress, psi
Value	-4922	2879	0.420	33	-118	55	157
				0.09[*]	0.47[*]	0.03[*]	0.17[*]
Failure Index	0.62	0.17	0.59	0.13[**]	0.59[**]	0.04[**]	0.21[**]

[*]Using typical strength value

[**]Using minimum strength value

In absence of the load ring termination in the spatial domain of the local model shown in Figure 29(a), the largest crush stress of 55 ksi occurred in the 8.1-pcf core in the proximity of the bottom boundary of the local model domain and it was likely affected by the global-local interface boundary effects. The most critical crush stress, predicted to occur in the 3.1-pcf core, was 33 ksi, which produced a failure index of 0.09 when calculated using the typical core crush strength. The most positive normal stress occurred at the termination of the last pad-up ply, but its magnitude was well within the allowable and far less than the equivalent values produced by the axisymmetric-element-based analysis in the perfect configuration at its incipient buckling. The normal stress values obtained from the local analysis domain at the locations other than those described above were well within allowables, did not exhibit large gradients, and were not significantly affected by accounting for the presence of radial imperfections in the analysis.

The largest transverse shear stresses shown in Figure 29(b), when the top and the bottom edges of the local domain are excluded from the consideration, were located at the last pad-up ply terminations. Similar to those derived from the crush stress results, substantial failure-index margins (significantly below the value of one) were still maintained. In general, however, the transverse shear response produced noticeably larger failure indices than those derived from the core crush results. While the acreage area showed more transverse shear stress fluctuations than the normal stress, the gradients were considered mild. When compared to the axisymmetric analysis results from the perfect model at incipient buckling, the imperfect global-local analysis produced smaller transverse shear stress peaks at the pad-up ply drops and the core density transitions.

Analysis of the core results obtained from the global-local model further affirmed that the axisymmetric-element-based analysis could not be relied upon to resolve very localized behavior in the transition zones, such as ply termination or core splicing, especially for the core crush behavior. While the global-local approach did not produce as extreme core results at the pad-up ply terminations as the axisymmetric-element-based analysis, it had been recognized that both analysis types applied the homogenized core modeling approach, which could have exceeded limits of its applicability when the behavior of interest was very localized and occurred on the scale comparable to or smaller than an individual core cell. Since the global-local analysis used more gradual modeling of ply drops in the pad-up area than the axisymmetric-element-based analysis, it was not possible to conclude whether this modeling feature or the type of elements used in the two analyses played the more important role affecting the results. Perhaps the most significant outcome of the global-local analysis was the observation that the core response was not sensitive to the geometric imperfections. Finally, as for the perfect cylinder axisymmetric-element-based analysis results, it was also recognized that no cumulative failure criterion measure that accounts for the combination of crush and transverse shear stress was available within the global-local analysis framework when the homogenized core modeling assumption was applied.

The facesheet response metrics obtained using the imperfect local model, and shown in Table 12, agreed well with those obtained from the imperfect shell-element-based model analysis, although both strain and Tsai-Hill index results predicted with the local model had slightly higher extrema than those from the shell-model analysis. The axial strain based on the local analysis domain was larger by 5.7% than that from the shell analysis, hoop strain by 4.2%, and Tsai-Hill index by 5.9%.

5.0 Concluding Remarks

The Shell Buckling Knockdown Factor Project has the goal of improving the buckling design guidelines for metallic and composite cylinders through high-fidelity analysis validated by large-scale testing. The presented work focused on the iterative design methodology for buckling critical large-scale sandwich composite test articles that would support the objective of developing validated high-fidelity analysis methods. The specific design challenge was to develop representative buckling-critical scaled test articles in the design-space of interest.

Overall, a practical engineering approach to support the design and analysis of large-scale buckling-critical test articles was devised that used custom-developed computational tools for closed-form preliminary design and analysis and a commercially available general-purpose finite element code to support the detailed design and analysis stage.

The first step in the multi-step test article design process was to define nondimensional geometric and stiffness parameters to determine the design space of interest. Next, a computationally efficient closed-form process was employed to evaluate a large pool of possible subscale test article designs. The initial downselection criteria involved determining designs that had global buckling as the first failure mode with a required margin separating this desired failure mode from other possible failure modes. The magnitude of the buckling load and the corresponding membrane compressive strain were constrained next. The span of the design space enveloped by the candidate test article designs (relative thinness and bending stiffness ratios) was also considered in this step of the process.

Finite element models were developed for a small number of downselected candidate test articles as a mean of enhancing the fidelity of the analysis over the closed-form approach. Several finite element analysis (FEA) methods were executed, including shell, axisymmetric, and global-local approaches, all relying ultimately on the geometrically nonlinear analyses. The shell FEA results allowed evaluation of the effects of the geometric manufacturing imperfections on the buckling loads and on the corresponding facesheet strains at buckling, which, along with the Tsai-Hill failure index, were used as a strength failure criterion. An axisymmetric FEA that allowed the assessment of the honeycomb-core performance, was undertaken next. Crush and transverse shear stresses were computed to ensure that these two failure modes were separated from the global buckling load by the required margin. However, this modelling approach was only applicable to the perfect cylinder geometry because of the axisymmetric assumption. To overcome this restriction, the core stresses for the imperfect cylinder configuration were also assessed using the global-local FEA, which is also referred to as the submodeling approach in the literature associated with the general-purpose FEA code Abaqus. While selecting local domains was not intuitive or objectively guided by quantitative criteria, the global-local FEA complemented the shell and axisymmetric FEA results in a meaningful way. The global-local results showed that the core crush and transverse shear stresses were not strongly affected by the cylinder geometric imperfections and the sandwich facesheet results contributed to developing confidence in the strain and Tsai-Hill failure criterion results obtained from the shell FEA.

6.0 References

1. Hilburger, M. W.: "Developing the Next Generation Shell Buckling Design Factors and Technologies," *Proceedings of the 53rd AIAA/ASME/ASCE/AHS/ASC Structures, Structural Dynamics and Materials Conference*, AIAA paper no. 2012-1686, Honolulu, HI, April 2012.
2. Sleight, D. W.; Kosareo, D. N.; and Thomas, S. D.: "Composite Interstage Structural Concept Down Select Process and Results," NASA NF1676L-13769, 2012, pp. 1-15.
3. Schultz, M. R.; Sleight, D. L.; Myers, D. E.; Waters, W. A. Jr.; Chunchu, P. B.; Lovejoy, A. E.; and Hilburger, M. W.: "Buckling Design and Imperfection Sensitivity of Sandwich Composite Launch-Vehicle Shell Structures," *Proceedings of the American Society for Composites: The 35th Technical Conference*, paper no. 3505, Williamsburg, VA, September 2016, DEStech Publications, Inc., CD-ROM.
4. Vinson, J. R.: *The Behavior of Sandwich Structures of Isotropic and Composite Materials*, Technomic, Lancaster, PA, 1999.
5. Hyer, M. W.: *Stress Analysis of Fiber-reinforced Composite Materials*, McGraw-Hill, New York, 1998.
6. Reese, C. D.; and Bert, C. W.: "Buckling of Orthotropic Sandwich Cylinders Under Axial Compression and Bending," *Journal of Aircraft*, vol. 11, 1974, pp. 207-212.
7. Hilburger, M. W.; Haynie, W. T.; Lovejoy, A. E.; Roberts, M. G.; Norris, J. P.; Waters, W. A.; and Herring, H. M.: "Subscale and Full-Scale Testing of Buckling-Critical Launch Vehicle Shell Structures," *Proceedings of the 53rd AIAA/ASME/ASCE/AHS/ASC Structures, Structural Dynamics and Materials Conference*, AIAA paper no. 2012-1688, Honolulu, HI, April 2012.
8. Schultz, M. R.; Sleight, D. L.; Gardner, N. W.; Rudd, M. T.; Hilburger, M. W.; Palm, T. E.; and Oldfield, N. J.: "Test and Analysis of a Buckling-Critical Large-Scale Sandwich Composite Cylinder," *Proceedings of the 58th AIAA/ASME/ASCE/AHS/ASC Structures, Structural Dynamics & Materials Conference*, AIAA paper no. 2018-1693, Orlando, FL, January 2018.
9. Lovejoy, A. E.; Hilburger, M. W.; Haynie, W. T.; Satyanarayana, A.; Gardner, N. W.; Roberts, M. G.; Norris, J. P.; and Thornburgh, R. P.: *Buckling Analysis and Test Results for Full-Scale 27.5-Foot-Diameter Integrally-Stiffened Al-Li Cylinder Test Articles*, NASA TM-2020-000000, 2020, Hampton, VA (in preparation).
10. Anonymous: *Buckling of Thin-Walled Circular Cylinders*, NASA SP-8007, September 1965, revised August 1968.
11. Abaqus/Standard, Software Package, Ver. 6.14-1, SIMULIA, Providence, RI, 2014.
12. Opliger, M.: SBKF testing results, electronic delivery, National Institute for Aviation Research, Wichita, KS, https://cop.ksc.nasa.gov/NESC/1693shell/SitePages/Home.aspx
13. Reeder, J. R.: "Property Values for Preliminary Design of the Ares I Composite Interstage," NASA internal memo to the Marshall Space Flight Center, NASA Langley Research Center, Hampton, VA, March 2007.
14. Anonymous: "HexWeb Honeycomb Attributes and Properties," Hexcel Composites, TSB 120, Pleasanton, CA, November 1999.
15. Bell, T.; Li, B.; and Zhang, S.: "Structured Light Techniques and Applications," article published in *Wiley Encyclopedia of Electrical and Electronics Engineering*, doi: 10.1002/047134608X.W8298, John Wiley and Sons, Inc., 2016.

16. Ivester, J.: *Shell Buckling CTA8.2 ATOS II Scan Data*, NASA internal report, version 2, MSFC, Huntsville, AL, August 8, 2017.
17. Kaw, A. K.: "Mechanics of Composite Materials," CRC, Taylor and Francis Group, Boca Raton, FL, Second Edition, 2006.

Appendix A. Summary of Analysis Results for CTA8.2B

The detailed CTA8.2B design included pad-ups in the facesheets and a higher density core at the cylinder ends to mitigate some of the high crush and shear stresses in the core associated with the load introduction. The pad-ups included up to four plies of the same Hexcel IM7/8552-1 tape used in the acreage facesheets: two +45° plies and two –45° plies that were interleaved with the acreage plies. The IML facesheet layups in the pad-up regions are shown in Table A1 where pad-up plies are listed in bold font. The OML facesheets were symmetric with the IML pad-ups. The thickness of the pad-up layers was built up away from the IML of the cylinder for both inner and outer facesheets because the cylinder was manufactured on a constant diameter tool. The transition from the 8.1-pcf core to the 3.1-pcf core, also shown in Table A1, occurred 10 in. from the cylinder ends, i.e. away from the pad-up ply terminations, to prevent interactions between core splices and pad-up ply terminations. Where the core sections were spliced, a width of approximately 0.25 in. (0.125 in. to both sides of the splice) was filled with an epoxy grout Hysol EA9396.6MD.

Table A1. CTA8.2B core transition and layups in acreage and pad-up regions.

CTA8.2B cylinder sections measured from cylinder ends, in.	Core Density, pcf	IML facesheet layup, degrees
Greater than 20 (Acreage)	3.1	[60/-60/0/0/-60/60]
18 to 20	3.1	[60/-60/**45**/0/0/-60/60]
14.5 to 18	3.1	[60/-60/**45**/0/0/-60/**-45**/60]
13.5 to 14.5	3.1	[60/-60/**45**/0/0/**45**/-60/**-45**/60]
10 to 13.5	3.1	[60/**-45**/-60/**45**/0/0/**45**/-60/**-45**/60]
0 to 10	8.1	[60/**-45**/-60/**45**/0/0/**45**/-60/**-45**/60]

*Bold font indicates a pad-up ply.

The predicted radial displacements from the perfect CTA8.2B analysis at incipient buckling is presented in Figure A1 and the corresponding axial strains in Figure A2. At the incipient buckling load, the cylinder was predicted to exhibit six rings of the outward radial displacements, four of which were within the acreage area, and one of which was in each the top and bottom pad-up areas. The maximum radial displacement of 0.13 in. was identified in the pad-up area. The maximum compressive strain of 5566 µε (Figure A2) was located in the IML facesheet of the acreage area within the dark blue band closest to pad-up section (only a negligible strain difference existed between the top and bottom symmetric locations).

The predicted radial displacements from the imperfect CTA8.2B analysis at incipient buckling is presented in Figure A3 and the corresponding axial strains in Figure A4. The imperfect cylinder was predicted to exhibit an incipient buckling response similar to that of the perfect configuration shown in Figure A1. Specifically, the predicted response of the imperfect cylinder had six outward radial displacement rings (albeit distorted rings), four of which were within the acreage area, and one of which was at each top and bottom pad-up areas. The four outward displacement rings within the acreage area were noticeably more distorted in shape that the two within the thicker pad-up areas. The maximum radial displacement of 0.11 in. was located in the pad-up area and was less than the 0.12 in. obtained for the perfect CTA8.2B model. This difference was largely attributed to the reduced buckling load of the imperfect cylinder. The maximum compressive strain was 5319 µε and was located in the IML facesheet acreage area close to the top pad-up termination (within one of the dark blue undulations seen just below the top pad-up termination line shown in Figure A4).
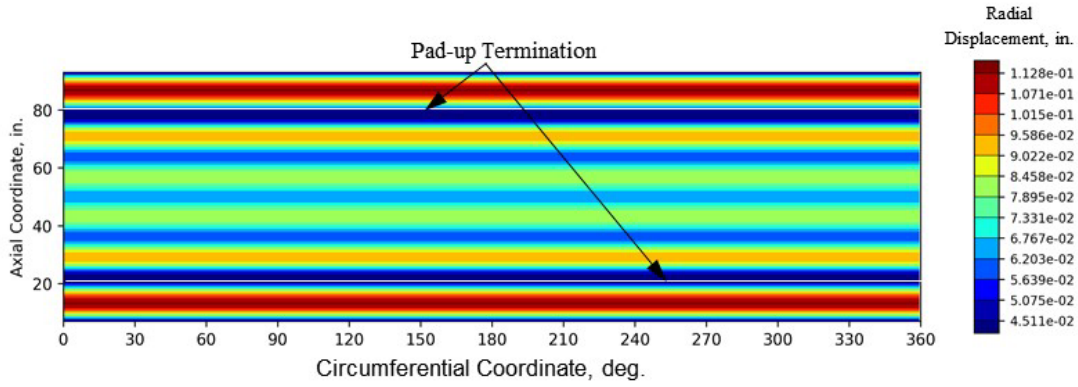
Figure A1. Perfect CTA8.2B radial displacement at incipient buckling.
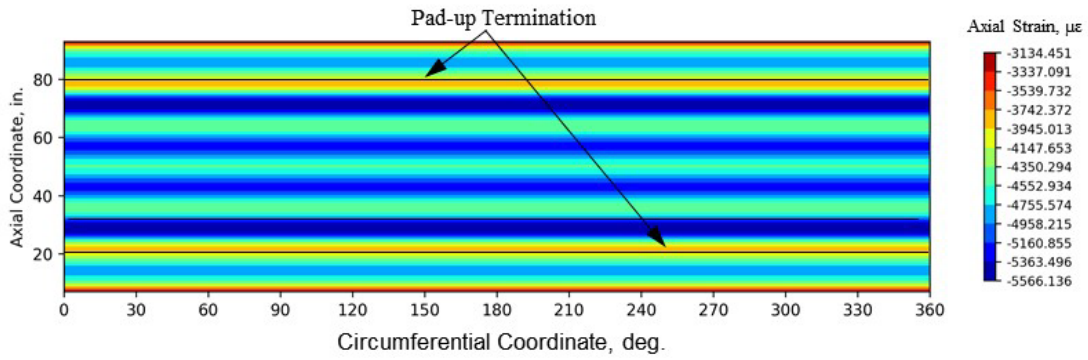

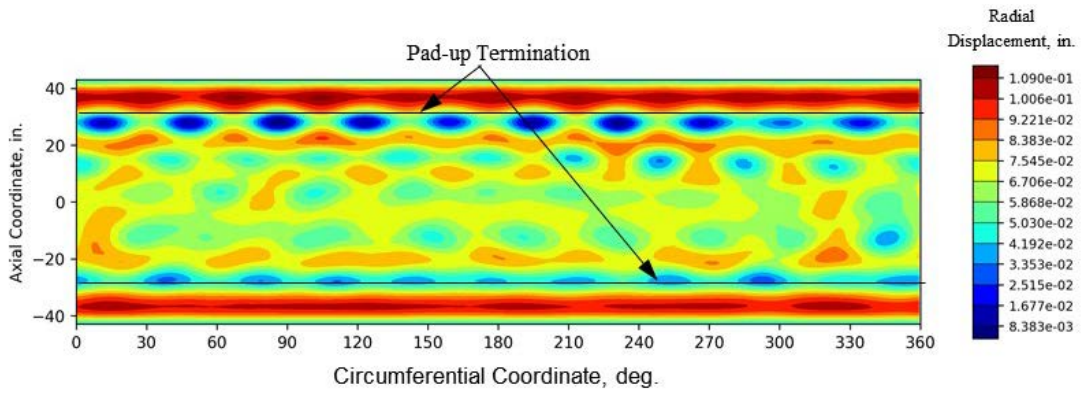Figure A2. Perfect CTA8.2B IML axial strain at incipient buckling.

Figure A3. Imperfect CTA8.2B radial displacement at incipient buckling.
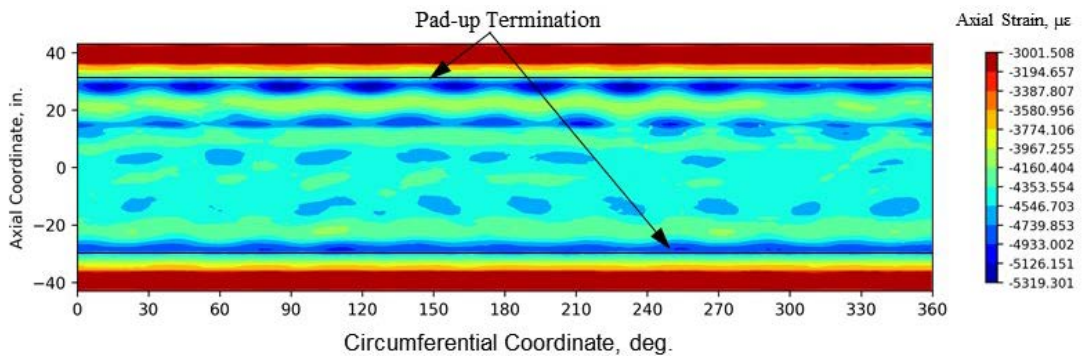

Figure A4. Imperfect CTA8.2B IML axial strain at incipient buckling.

A summary of strain and Tsai-Hill indices is shown in Table A2 and these measures are accompanied by the corresponding failure indices. For the three metrics considered in Table A2, the imperfect cylinder configurations produced the results that were less extreme than those of the perfect model. This behavior was attributed to the reduced buckling load of the imperfect configuration.

Table A2. Summary of the shell-element-based results for the CTA8.2B perfect model at 942 kips and imperfect model at 863 kips.

Measure, Unit	Axial Strain, με		Hoop Strain, με		Tsai-Hill Index	
Model	Perfect	Imperfect	Perfect	Imperfect	Perfect	Imperfect
Value	-5566	-5319	2384	2289	0.491	0.464
Failure Index	0.70[*]	0.67[*]	0.14[**]	0.13[**]	0.69[***]	0.65[***]

[*] Computed using -7926 με compression allowable

[**] Computed using 17,400 με tension allowable

[***] Computed using 0.71 co-cure sandwich knockdown factor (reference Appendix E).

The results obtained from the axisymmetric perfect CTA8.2B analysis are presented in Table A3. Only the nominal sliding boundary condition in Table A3 had all the predicted failure indices less than unity in the 8.1-pcf core material at the ends of the cylinder. If a full or partial adhesive bond were to develop during the manufacturing process between the test article and the load introduction metallic ring, and that bond was not broken at subcritical load levels, the CTA8.2B test article could suffer premature failure due to core crushing (under both the tied and sliding IML/tied OML boundary assumptions) or due to the transverse core shearing (under the sliding IML/tied OML boundary assumption).

Table A3. Perfect CTA8.2B model crush and transverse shear stresses in the 8.1-pcf core for different boundary condition modeling in the axisymmetric-element-based model at 948 kips.

End Boundary Condition	Crush Stress, psi	Failure Index		Transverse Shear Stress Loc. 1, psi	Failure Index		Transverse Shear Stress Loc. 2, psi	Failure Index	
		Typical	Min.		Typical	Min.		Typical	Min.
Tied	2452	1.29	1.89	270	0.29	0.36	-701	0.74	0.95
Sliding	625	0.33	0.48	231	0.24	0.31	-216	0.23	0.29
Sliding IML/ Tied OML	1831	0.96	1.41	315	0.33	0.43	-760	0.80	1.03

[*]General locations 1 and 2 per Figure 21.

Overall, when considering all the damage modes presented in Table A2 and the nominal sliding end boundary results in Table A3, the larger failure indices were produced by the axial compression of the IML facesheet in the acreage section of the test article.

Appendix B. Summary of Analysis Results for CTA8.4

The detailed CTA8.4 design included pad-ups in the facesheets and a higher density core at the cylinder ends to mitigate some of the high crush and shear stresses in the core associated with the load introduction. The pad-ups included up to six plies of the same Hexcel IM7/8552-1 tape used in the acreage facesheets: three +45° plies and three –45° plies that were interleaved with the acreage plies. The IML facesheet layups in the pad-up regions are shown in Table B1 where pad-up plies are listed in bold font. The OML facesheets were symmetric with the IML pad-ups. The thickness of the pad-up layers was built up away from the IML of the cylinder for both inner and outer facesheets because the cylinder was manufactured on a constant diameter tool. The transition from the 8.1-pcf core to the 3.1-pcf core, also shown in Table B1, occurred 10 in. from the cylinder ends, i.e. away from the pad-up ply terminations, to prevent interactions between core splices and pad-up ply terminations. Where the core sections were spliced, a width of approximately 0.25 in. (0.125 in. to both sides of the splice) was filled with an epoxy grout Hysol EA9396.6MD.

Table B1. CTA8.4 core transition and layups in acreage and pad-up regions.

CTA8.4 cylinder sections measured from cylinder ends, in.	Core Density, pcf	IML facesheet layup, degrees
Greater than 20 (Acreage)	3.1	[30/-30/90/0/0/90/-30/30]
19 to 20	3.1	[30/-30/**45**/90/0/0/90/-30/30]
18 to 19	3.1	[30/-30/**45**/**-45**/90/0/0/90/-30/30]
17 to 18	3.1	[30/-30/**45**/**-45**/90/45/0/0/90/**45**/-30/30]
15.5 to 17	3.1	[30/-30/**45**/**-45**/90/0/0/90/**-45**/**45**/-30/30]
14 to 15.5	3.1	[30/-30/**45**/**-45**/90/0/**45**/0/90/**-45**/**45**/-30/30]
10 to 14	3.1	[30/-30/**45**/**-45**/90/0/**45**/**-45**/0/90/**-45**/**45**/-30/30]
0 to 10	8.1	[30/-30/**45**/**-45**/90/0/**45**/**-45**/0/90/**-45**/**45**/-30/30]

*Bold font indicates a pad-up ply.

The predicted radial displacements from the perfect CTA8.4 analysis at incipient buckling is presented in Figure B1, and the corresponding axial strains in Figure B2. At the incipient buckling load, the cylinder was predicted to exhibit two well-defined rings of the outward radial displacements just outside the pad-up areas, and smaller-amplitude and nonaxisymmetric displacements within the acreage area farther away from the pad-ups. The maximum radial displacement of 0.13 in. was identified in the pad-up area. The maximum compressive strain of 5084 με (Figure B2) was located in the IML facesheet of the acreage area within the dark blue band closest to the pad-up section (only a negligible strain difference existed between the top and bottom symmetric locations).

The predicted radial displacements from the imperfect CTA8.4 analysis at incipient buckling is presented in Figure B3 and the corresponding axial strains in Figure B4. At incipient buckling the cylinder exhibited a response similar to the perfect configuration shown in Figures B1 and B2 but with more localized radial displacements and axial strains, which, however, still occurred as organized in a relatively regular grid pattern. The maximum radial displacement of 0.12 in. was located in the pad-up area and was comparable to that of the perfect CTA8.4 model. The maximum compressive strain of 5021 με was also similar to that of the perfect model and was located in the IML facesheet acreage area close to the top pad-up termination around the 120° circumferential coordinate, as shown in Figure B4.
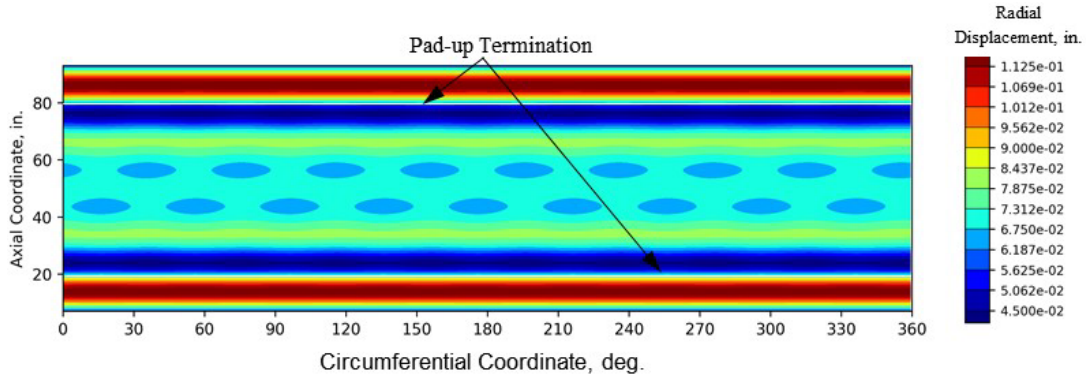
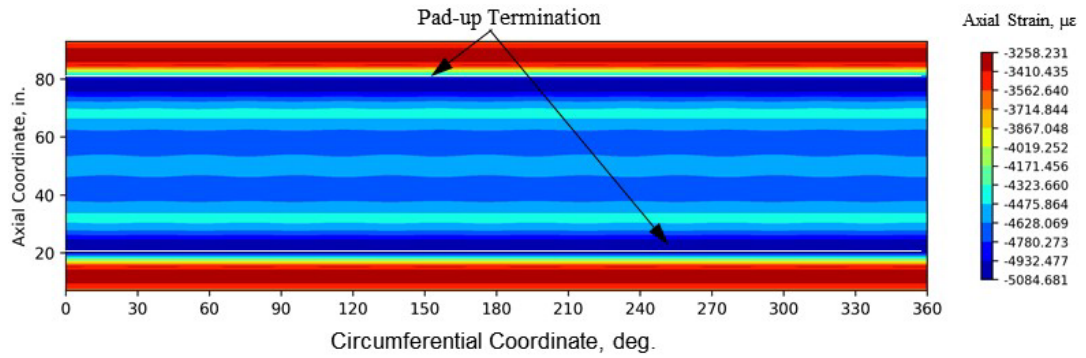Figure B1. Perfect CTA8.4 radial displacement at incipient buckling.

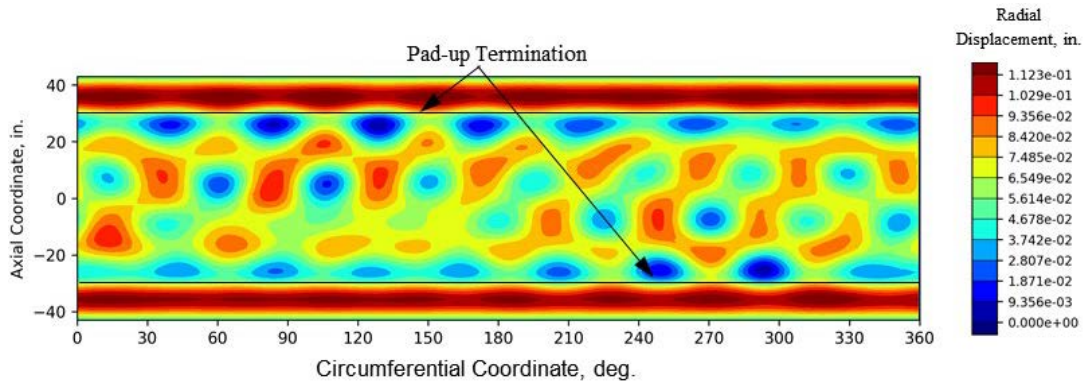Figure B2. Perfect CTA8.4 IML axial strain at incipient buckling.

Figure B3. Imperfect CTA8.4 radial displacement at incipient buckling.
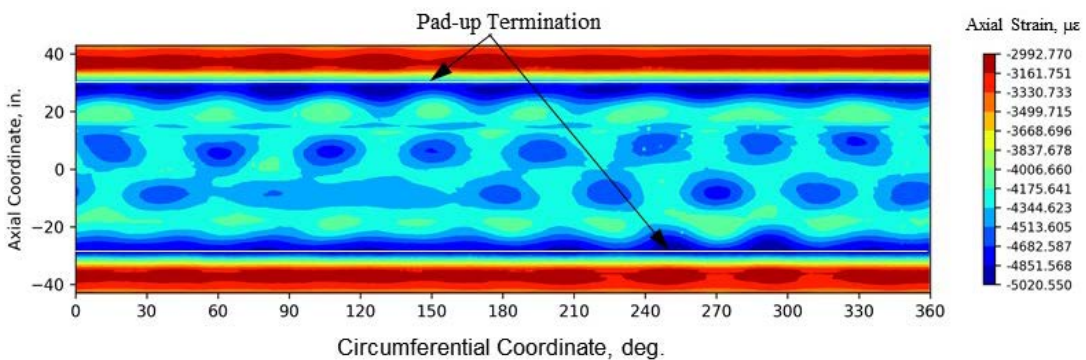

Figure B4. Imperfect CTA8.4 IML axial strain at incipient buckling.

A summary of strain and Tsai-Hill indices is shown in Table B2 and these measures are accompanied by the corresponding failure indices. For the three metrics considered in Table B2, the perfect and imperfect cylinder configurations produced results that did not differ significantly. It is speculated that this result was, at least in part, attributed to the thicker core (0.3 in.) when compared with the analysis results from the CTA8.2B and CTA8.3 test articles with a thinner core (0.2 in.). The increased bending stiffness of the CTA8.4 design made this configuration relatively less affected by the imperfections because the magnitudes of the radial and thickness imperfections were not scaled with the increased sandwich wall thickness.

Table B2. Summary of the shell-element-based results for the CTA8.4 perfect model at 1312 kips and imperfect model at 1241 kips.

Measure, Unit	Axial Strain, με		Hoop Strain, με		Tsai-Hill Index	
Model	Perfect	Imperfect	Perfect	Imperfect	Perfect	Imperfect
Value	-5085	-5021	2442	2509	0.449	0.442
Failure Index	0.64[*]	0.63[*]	0.14[**]	0.14[**]	0.63[***]	0.62[***]

[*] Computed using -7926 με compression allowable

[**] Computed using 17,400 με tension allowable

[***] Computed using 0.71 co-cure sandwich knockdown factor (reference Appendix E)

The results obtained from the axisymmetric perfect CTA8.4 analysis are presented in Table B3. In Table B3, only the nominal sliding boundary condition had all the predicted failure indices less than unity in the 8.1-pcf core material at the ends of the cylinder. If a full or partial adhesive bond developed during the manufacturing process between the test article and the load introduction metallic ring, and that bond did not break at subcritical load levels, the CTA8.4 test article could suffer premature failure due to core crushing (under both tied and sliding IML/tied OML boundary assumption). The 8.1-pcf core was not predicted to fail due to the transverse shearing even under the off-nominal boundary assumptions.

Overall, when considering all the damage modes presented in Table B2 and the nominal sliding end boundary results in Table B3, the larger failure indices were produced by the axial compression of the IML facesheet in the acreage section of the test article.

Table B3. Perfect CTA8.4 model crush and transverse shear stresses in the 8.1-pcf core for different boundary condition modeling in the axisymmetric-element-based model at 1311 kips.

End Boundary Condition	Crush Stress, psi	Failure Index		Transverse Shear Stress Loc. 1, psi	Failure Index		Transverse Shear Stress Loc. 2, psi	Failure Index	
		Typical	Min.		Typical	Min.		Typical	Min.
Tied	2450	1.29	1.88	287	0.30	0.39	-538	0.56	0.73
Sliding	612	0.32	0.47	232	0.25	0.31	-150	0.16	0.20
Sliding IML/ Tied OML	1854	0.98	1.43	337	0.36	0.46	-623	0.66	0.84

[*]General locations 1 and 2 per Figure 21.

Appendix C. Summary of Analysis Results for CTA8.5

The detailed CTA8.5 design included pad-ups in the facesheets and a higher density core at the cylinder ends to mitigate some of the high crush and shear stresses in the core associated with the load introduction. The pad-ups included up to six plies of the same Hexcel IM7/8552-1 tape used in the acreage facesheets: three +45° plies and three –45° plies that were interleaved with the acreage plies. The IML facesheet layups in the pad-up regions are shown in Table C1 where pad-up plies are listed in bold font. The OML facesheets were symmetric with the IML pad-ups. The thickness of the pad-up layers was built up away from the IML of the cylinder for both inner and outer facesheets because the cylinder was manufactured on a constant diameter tool. The transition from the 8.1-pcf core to the 3.1-pcf core, also shown in Table C1, occurred 10 in. from the cylinder ends, i.e. away from the pad-up ply terminations, to prevent interactions between core splices and pad-up ply terminations. Where the core sections were spliced, a width of approximately 0.25 in. (0.125 in. to both sides of the splice) was filled with an epoxy grout Hysol EA9396.6MD.

Table C1. CTA8.5 core transition and layups in acreage and pad-up regions.

CTA8.5 cylinder sections measured from cylinder ends, in.	Core Density, pcf	IML facesheet layup, degrees
Greater than 20 (Acreage)	3.1	[90/0/90/0/-30/30/90/90/0]
19 to 20	3.1	[90/0/**-45**/90/0/-30/30/90/90/0]
18 to 19	3.1	[90/0/**-45**/**45**/90/0/-30/30/90/90/0]
17 to 18	3.1	[90/0/**-45**/**45**/90/0/**45**/-30/30/90/90/0]
15.5 to 17	3.1	[90/0/**-45**/**45**/90/0/**-45**/**45**/-30/30/90/90/0]
14 to 15.5	3.1	[90/0/**-45**/**45**/90/0/**-45**/**45**/-30/30/90/**-45**/90/0]
10 to 14	3.1	[90/0/**-45**/**45**/90/0/**-45**/**45**/-30/30/90/**-45**/**45**/90/0]
0 to 10	8.1	[90/0/**-45**/**45**/90/0/**-45**/**45**/-30/30/90/**-45**/**45**/90/0]

*Bold font indicates a pad-up ply.

The predicted radial displacement at incipient buckling for the perfect CTA8.5 analysis is presented in Figure C1 and the corresponding axial strains in Figure C2. At the incipient buckling load, the cylinder was predicted to exhibit two well-defined rings of the outward radial displacements just outside the pad-up areas, and smaller-amplitude and nonaxisymmetric displacements within the acreage area farther away from the pad-ups. The maximum radial displacement of 0.05 in. was identified in the pad-up area and was significantly smaller than in the other designs considered. This difference was due to the facesheet layup approaching a cross-ply layup, i.e., producing significant axial and hoop stiffness at the expense of the inplane shear stiffness. The maximum compressive strain of 4484 µε (Figure C2) was located in the IML facesheet of the acreage area within the dark blue band closest to pad-up section (only a negligible strain difference existed between the top and bottom symmetric locations).

The predicted radial displacements at incipient buckling for the imperfect CTA8.5 analysis is presented in Figure C3 and the corresponding axial strains in Figure C4. At incipient buckling the cylinder was predicted to exhibit a response with well-defined localized radial displacement and axial strain orthogonal grids. The maximum radial displacement of 0.05 in. was located in the pad-up area and was comparable to that of the perfect CTA8.5 model. The maximum compressive strain of 4470 µε was also similar to that of the perfect model, but was located in the IML facesheet acreage area further away from the pad-up sections, as shown in Figure C4.
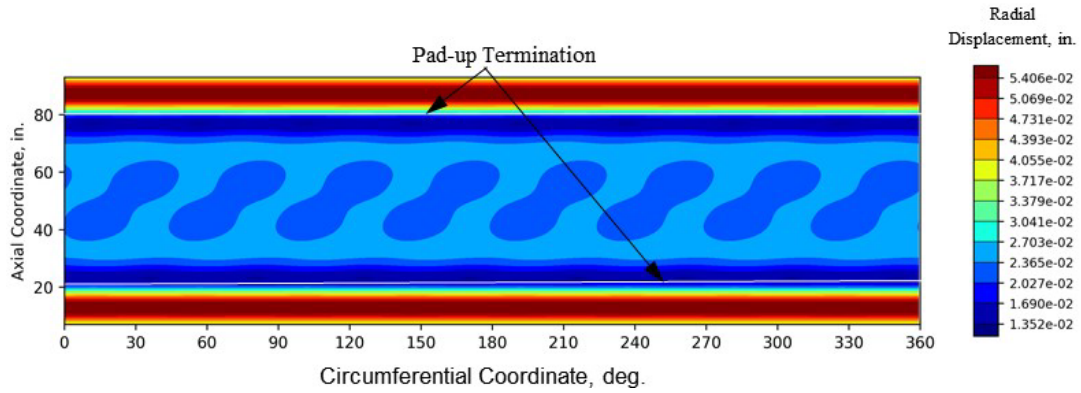
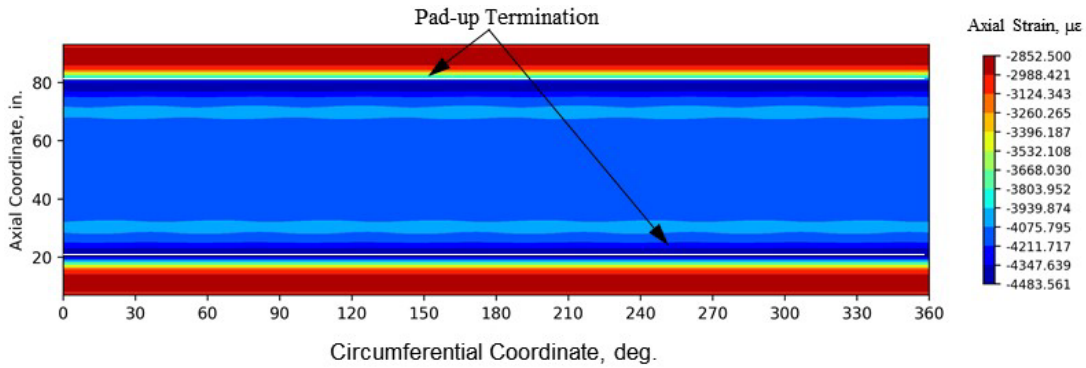Figure C1. Perfect CTA8.5 radial displacement at incipient buckling.

Figure C2. Perfect CTA8.5 IML axial strain at incipient buckling.
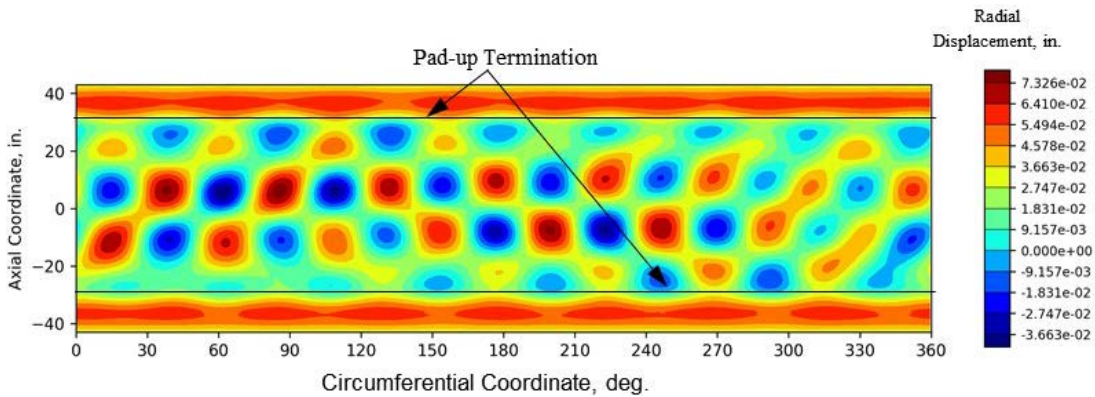

Figure C3. Imperfect CTA8.5 radial displacement at incipient buckling.
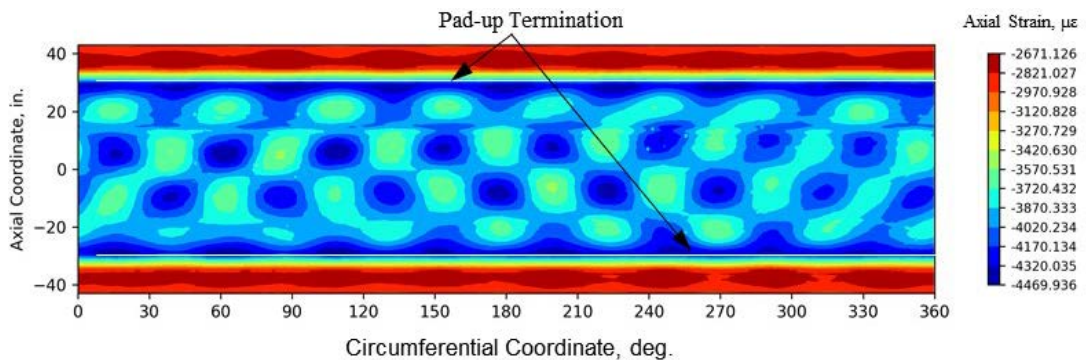

Figure C4. Imperfect CTA8.5 IML axial strain at incipient buckling.

A summary of strain and Tsai-Hill indices from the perfect and imperfect CTA8.5 models is shown in Table C2 and these measures are accompanied by the corresponding failure indices. For the three metrics considered in Table C2, the perfect and imperfect cylinder configurations produced results that did not differ significantly. It is speculated that this result had the similar underlying cause as the one for CTA8.4 (Appendix B), namely, the thicker 0.3-in. core than that of the CTA8.2B and CTA8.3 test articles (0.2 in.). The increased bending stiffness of the CTA8.5 design made this configuration relatively less affected by the imperfections because the magnitudes of the radial and thickness imperfections were not scaled with the increased sandwich wall thickness. Of note in Table C2 are also low levels of the tensile hoop strains when compared to other designs. This result was attributed to the facesheet layup approaching a cross-ply layup, which had higher hoop stiffness than other designs.

Table C2. Summary of the shell-element-based results for the CTA8.5 perfect model at 1205 kips and imperfect model at 1156 kips.

Measure, Unit	Axial Strain, µε		Hoop Strain, µε		Tsai-Hill Index	
Model	Perfect	Imperfect	Perfect	Imperfect	Perfect	Imperfect
Value	-4484	-4470	1209	1265	0.400	0.398
Failure Index	0.57[*]	0.56[*]	0.07[**]	0.07[**]	0.56[***]	0.56[***]

[*] Computed using -7926 µε compression allowable

[**] Computed using 17,400 µε tension allowable

[***] Computed using 0.71 co-cure sandwich knockdown factor (reference Appendix E)

The results obtained from the axisymmetric perfect CTA8.5 analysis are presented in Table C3. The nominal sliding boundary condition in Table C3 had all the predicted failure indices less than unity in the 8.1-pcf core material at the ends of the cylinder. If a full or partial adhesive bond developed during the manufacturing process between the test article and the load introduction metallic ring, and that bond did not break at subcritical load levels, the CTA8.5 test article could suffer premature failure due to core crushing under both tied and sliding IML/tied OML boundary assumption. The 8.1-pcf core was not predicted to fail due to the transverse shearing even under the off-nominal boundary assumptions.

Overall, when considering all the damage modes presented in Table C2 and the nominal sliding end boundary results in Table C3, the larger failure indices were produced by the axial compression of the IML facesheet in the acreage section of the test article.

Table C3. Perfect CTA8.5 model crush and transverse shear stresses in the 8.1-pcf core for different boundary condition modeling in the axisymmetric-element-based model at 1198 kips.

End Boundary Condition	Crush Stress, psi	Failure Index		Transverse Shear Stress Loc. 1, psi	Failure Index		Transverse Shear Stress Loc. 2, psi	Failure Index	
		Typical	Min.		Typical	Min.		Typical	Min.
Tied	1977	1.04	1.52	210	0.22	0.28	-292	0.31	0.39
Sliding	342	0.18	0.26	148	0.16	0.20	-77	0.08	0.11
Sliding IML/ Tied OML	1521	0.80	1.17	304	0.32	0.41	-447	0.47	0.60

[*]General locations 1 and 2 per Figure 21.

Appendix D. Work Calculated along Global-Local Model Interfaces

The work measures produced for the nodes belonging to the global and local domains were computed for the perfect CTA8.2B global-local model individually for all four boundary edges between the two spatial domains, as depicted with the local model shown in red in Figure D1. The work performed by the nodes of the global model included products of nodal forces and translations and nodal moments and rotations, because those were all active in the shell elements of the global domain. For the nodes belonging to the local model, only the products of forces and translations contributed to the work, as no rotational degrees of freedom were active in the solid and continuum shell elements of the local domain.

The total work along the four global-local model interfaces is shown in Table D1. The results indicate that the largest work was performed by the nodes along Interface 1 near the top of the model. This result was intuitive, as Interface 1 was very close to the applied axial displacement making the displacements along this interface the largest among the four interfaces considered. Interface 1 was also the interface that showed the largest work difference of 2.9% between the global and local domains. The work performed by the nodes at Interface 3 was the lowest of the four interfaces. This result was also intuitive as Interface 3 was very close to the constrained end of the model, resulting in small nodal displacements. Interface 3 showed the work difference of -1.7%. Interfaces 1 and 3 transferred the loads in the axial direction which is the main loading direction of the cylinder. Since the work differences between the global and local domains along Interfaces 1 and 3 were small and had opposite signs, and the work differences between the side Interfaces 2 and 4 were negligible, it was judged that the automated Abaqus algorithm with the default settings for connecting global and local domains was an acceptable approach for the problem under consideration.
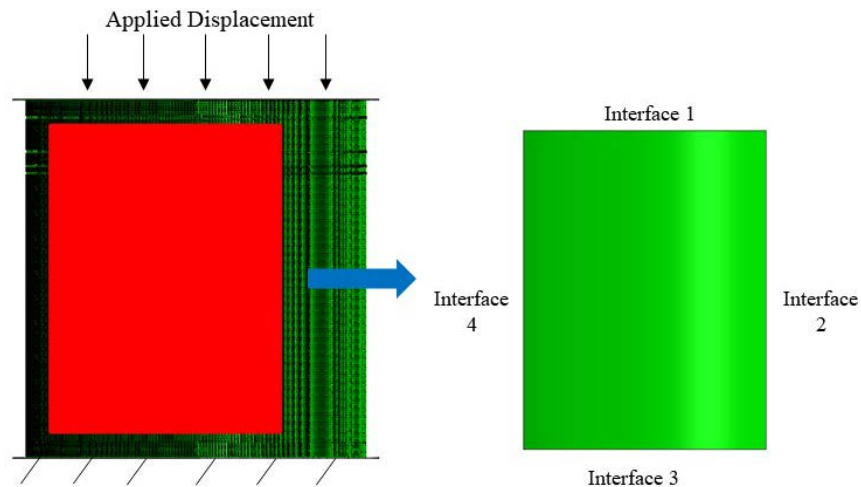

Figure D1. Global-local model interfaces used to compute nodal work measures.

Table D1. Work along the global-local domain interfaces of the perfect CTA8.2B model at 794 kips.

Interface	Work, in. x lbf		Difference, %
	Global Model	Local Model	
1	67,921	66,033	2.9
2	32,246	32,212	0.1
3	1645	1673	-1.7
4	32,252	32,339	-0.3

Appendix E. Co-cure Knockdown Factor

A co-cure knockdown factor is often used to account for the reduction of laminate properties for laminates that are co-cured on a sandwich core rather than as a monocoque composite cured on a solid tool. This reduction of stiffness and strength properties can typically result from the facesheet undulations or dimples due to laying it over nonhomogeneous and/or uneven core, such as in the honeycomb-core cells, and/or using lower pressure in the cure process not to exceed the crush core allowables. The co-cure knockdown (KD) factor was defined as[E1]

$$KD\ Factor = \frac{\sigma_{cc}}{\sigma} \tag{E1}$$

where σ_{cc} is the co-cure compressive strength of facesheet and σ is the compressive strength without co-cure imperfections.

Based on a literature survey[E1-E4] a typical knockdown factor for comparable sandwich composites was determined to be between 0.50 and 0.75. An independent derivation of the co-cure knockdown factor was undertaken initially for the CTA8.2B design with the facesheet laminate shown in Table 1. First, Equation (E1) was recast in terms of the compressive strength of laminae as

$$KD\ Factor = \frac{\sigma_U}{X_C} \tag{E2}$$

where σ_U is the facesheet lamina strength and X_C is the compressive lamina strength, both in fiber direction. Next, based on the mechanics of materials and the rule-of-mixtures approach, the unidirectional lamina axial strength, σ_U, was expressed as[E5]

$$\sigma_U = \frac{\sigma_x - E_0 \varepsilon_x (1-V)}{V} \tag{E3}$$

where σ_x is measured angle-ply lamina strength, E_0 axial modulus of the $\pm 60°$ laminae material, ε_x measured angle-ply laminate axial strain at failure, and V volume fraction of axial laminae (0°). After substituting Equation (E3) into (E2), and using data from References E6 and E7, the KD Factor of 0.71 was obtained and used for all test articles. Of note is that the derived factor fell within the limits established from the literature survey.

References
E1   Nettles, A.: "Some Examples of the Relation Between Processing and Damage Tolerance," *https://ntrs.nasa.gov/archive/nasa/casi.ntrs.nasa.gov/20130000533.pdf*
E2   Campbell, F. C.: "Manufacturing Processes for Advanced Composites," Chapter 8, Elsevier Advanced Technology, Oxford, UK, 2004.
E3   Collet, A.: *Cylindrical Test Article Design for NESC Shell Buckling Knockdown Factors Assessment*, Report TR023120, ATK Space Systems, Clearfield, UT, April 2008.
E4   Zhou, X.: *Characterization and Validation of Material Knockdown Factors for Sandwich Structures*, White Paper, ATK Mission Systems, Clearfield, UT, February 2008.
E5   Welsh, J. S.; and Adams, D. F.: "Testing of Angle-Ply Laminates to Obtain Unidirectional Composite Compression Strength," *Composites Part A*, Vol. 28(A), 1997, pp. 387-396.
E6   Opliger, M.: SBKF testing results, electronic delivery, National Institute for Aviation Research, Wichita, KS, https://cop.ksc.nasa.gov/NESC/1693shell/SitePages/Home.aspx
E7   Reeder, J. R.: "Property Values for Preliminary Design of the Ares I Composite Interstage," NASA internal memo to the Marshall Space Flight Center, NASA Langley Research Center, Hampton, VA, March 2007.

REPORT DOCUMENTATION PAGE

1. REPORT DATE *(DD-MM-YYYY)*	2. REPORT TYPE	3. DATES COVERED *(From - To)*
01/11/2020	Technical Memorandum	07/01/2015 - 4/30/2018

4. TITLE AND SUBTITLE

Design and Analysis of Buckling-Critical Large-Scale Sandwich Composite Cylindrical Test Articles

5a. CONTRACT NUMBER

5b. GRANT NUMBER

5c. PROGRAM ELEMENT NUMBER

6. AUTHOR(S)

Przekop, Adam; Schultz, Marc R.; Kosztowny, Cyrus J.; Song, Kyongchan; Lindell, Michael C.; Hilburger, Mark W.; Rudd, Michelle T.

5d. PROJECT NUMBER

5e. TASK NUMBER

5f. WORK UNIT NUMBER

869021.04.23.01.13

7. PERFORMING ORGANIZATION NAME(S) AND ADDRESS(ES)

NASA Langley Research Center, Hampton, VA;
NASA Marshall Space Flight Center, Huntsville, AL

8. PERFORMING ORGANIZATION REPORT NUMBER

9. SPONSORING/MONITORING AGENCY NAME(S) AND ADDRESS(ES)

National Aeronautics and Space Administration
Washington, DC 20546-0001

10. SPONSOR/MONITOR'S ACRONYM(S)

NASA

11. SPONSOR/MONITOR'S REPORT NUMBER(S)

NASA/TM-20205008667

12. DISTRIBUTION/AVAILABILITY STATEMENT

Unclassified - Unlimited
Subject Category Space Transportation and Safety
Availability: NASA STI Program (757) 864-9658

13. SUPPLEMENTARY NOTES

The work described in this report was conducted as part of the NASA Engineering and Safety Center (NESC) Shell Buckling Knockdown Factor Project, NESC assessment number 07-010-E.

14. ABSTRACT

The test article design methodology for large-scale, honeycomb-core sandwich composite cylinder validation tests is discussed and cylinder designs are presented. First, the sandwich composite design space was defined using several nondimensional parameters, and the desired test article design space was determined by examining the designs of launch-vehicle cylinder structures. Selected designs that spanned a significant portion of the design space of interest and had global buckling as the first predicted failure mode were selected and subjected to higher-fidelity finite element analyses: shell-element-based analyses, axisymmetric-element-based analyses, and global-local analyses.

15. SUBJECT TERMS

Large-scale testing; sandwich composite cylinders; buckling; closed-form analysis; finite element analysis

16. SECURITY CLASSIFICATION OF:			17. LIMITATION OF ABSTRACT	18. NUMBER OF PAGES	19a. NAME OF RESPONSIBLE PERSON
a. REPORT	b. ABSTRACT	c. THIS PAGE			STI Help Desk (email: help@sti.nasa.gov)
U	U	U	UU	64	19b. TELEPHONE NUMBER *(Include area code)* (757) 864-9658